

# Anomalous Underscreening in the Restricted Primitive Model

Andreas Härtel,<sup>1,\*</sup> Moritz Bültmann,<sup>1</sup> and Fabian Coupette<sup>1</sup>

<sup>1</sup>*Institute of Physics, University of Freiburg, Hermann-Herder-Straße 3, 79104 Freiburg, Germany*  
(Published in: Physical Review Letters **130**, 108202 (2023), DOI: 10.1103/PhysRevLett.130.108202)

Underscreening is a collective term for charge correlations in electrolytes decaying slower than the Debye length. Anomalous underscreening refers to phenomenology that cannot be attributed alone to steric interactions. Experiments with concentrated electrolytes and ionic fluids report anomalous underscreening, which so far has not been observed in simulation. We present Molecular Dynamics simulation results exhibiting anomalous underscreening that can be connected to cluster formation. A theory that accounts for ion pairing confirms the trend. Our results challenge the classic understanding of dense electrolytes impacting the design of technologies for energy storage and conversion.

In recent years, unexpectedly long decay lengths of electrostatic forces have been observed in concentrated electrolytes [1–8] subsumed under the term “underscreening”. A lot of effort has been committed to explaining underscreening [9–25]. We distinguish regular underscreening that can be attributed to steric interactions from anomalous underscreening characterized by much longer decay lengths compared to its regular counterpart. Numerous studies have concluded that one of the most fundamental models for electrolytes and ionic liquids, the restricted primitive model (RPM), does not exhibit anomalous underscreening. As even some experimental studies could not find these large decay lengths [25, 26], the phenomenon itself has been questioned. In this Letter, we demonstrate that there is anomalous underscreening in the RPM using Molecular Dynamics simulations. However, our findings do not support a unique scaling of decay lengths as reported in [10, 11]. We can explain our directly measured results with cluster formation, which effectively reduces the concentration of mobile charge carriers. Finally, we propose a minimal theory of ion pairing that captures the phenomenology and even provides sensible agreement with the experiment.

In an ionic fluid, the Coulomb interaction between two charged particles is exponentially screened due to the presence of mobile charge carriers. The screening length is the inverse decay rate of this exponential, which reflects the ability of an electrolyte to screen surface charges on electrodes. Accordingly, it is closely related to the formation of electric double layers, which play a fundamental role in, among others, modern charge storing, energy conversion, and desalination technologies [27–30], chemical and colloidal interactions [31–33], and DNA [34, 35], as well as nervous conduction [36, 37]. The strength of electrostatic interactions is encoded in the Bjerrum length  $\lambda_B = e^2/(4\pi\epsilon_0\epsilon k_B T)$ , with elementary charge  $e$ , vacuum permittivity  $\epsilon_0$ , the relative dielectric permittivity of the solvent  $\epsilon$ , and Boltzmann’s constant  $k_B$ .

The expected decay length for dilute systems of charged particles is given by the Debye screening length

$\lambda_D = 1/\sqrt{8\pi\rho_s\lambda_B}$  [38] that decreases with increasing number density  $\rho_s$  of mobile charges and with the Bjerrum length. By convention  $\rho_s$  is the individual density of positive and negative charges, respectively, and often given as salt concentration  $c$ . Underscreening refers to a less effective screening, i.e., decay lengths exceeding the Debye length that have been observed by surface force apparatus (SFA) experiments for high salt concentrations or large Bjerrum lengths [1].

However, the experiments report that the charge correlation is the sum of two qualitatively different decays: a potentially oscillatory structural decay at small distances and a much slower long-ranged strictly nonoscillatory decay at greater separations [39]. The structural decay is well understood theoretically within the RPM of charged hard spheres and originates from the interplay between electrostatic and steric interactions of the particles (see [24] and references therein).

From simulations of the monovalent RPM, we can extract the charge correlation as  $h_{cc} = g_{++} - g_{+-}$ , where  $g_{\mu\nu}$  denotes the species resolved pair-distribution function. In theory, these pair-distribution functions can be obtained from the Ornstein-Zernike equation that defines their analytic structure. The charge correlation can be expressed as an infinite sum over terms of the form

$$H_i(r) = A_i \exp(-r/\lambda_i) \cos(\omega_i r + \tau_i)/r^{b_i} \quad (1)$$

with decay or screening length  $\lambda_i$ , amplitude  $A_i$ ,  $\omega_i$  and  $\tau_i$  describing potential oscillations, and  $b_i \in \{1, 2\}$ . Each term originates from a complex singularity of an auxiliary function,  $b_i = 1$  applies for simple poles [40–43], and  $b_i = 2$  for branch points [44, 45]. Further details are given in the Supplemental Material [46]. At long separations  $r$  the contribution with the longest decay length  $\lambda_i$  dominates. With increasing salt concentration, the dominant exponential decay switches from monotonic to oscillatory (Kirkwood crossover) [61, 62] as well as from charge to density dominated [15], depending on the ionic diameter.

It needs to be emphasized that the structural decay observed in the experiments already shows underscreening. This *regular* underscreening has been observed in simulations and the underlying mechanism is theoretically well understood.

\* andreas.haertel@physik.uni-freiburg.de

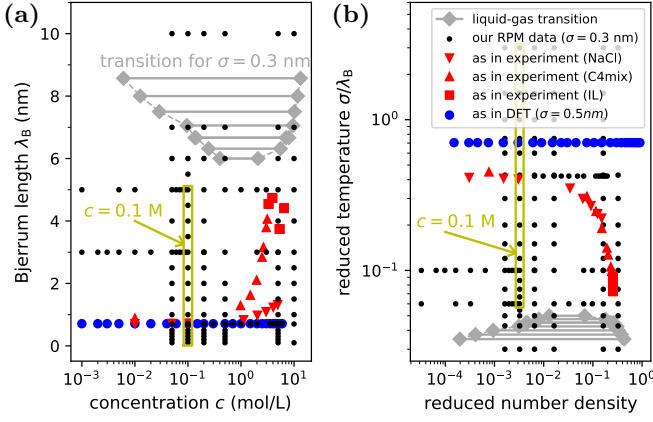


Figure 1. Phase diagram of the RPM for (a) the concentration  $c$  and Bjerrum length  $\lambda_B$  and (b) for reduced temperature  $T^* = \sigma/\lambda_B$  and total number density  $\rho^* = 2\rho_s\sigma^3$ . Each symbol marks a parameter set for which we have run MD simulations. The data points for  $c = 0.1$  mol/L and  $\lambda_B = 0.1 \dots 5.0$  nm are highlighted by an orange rectangle. Special symbols show the sets used in a previous theoretical study (DFT) [24] and in experiments [5] with NaCl in water (NaCl), [C4C1Pyr][NTf2] in propylene carbonate (C4mix), and an ionic liquid (IL) (further details in the Supplemental Material [46]). Horizontal lines mark the region of liquid-gas phase coexistence [63]; see [64] for further phases.

In contrast to that, the long-ranged decay was found exclusively in a few experimental studies. Recent works concluded that the RPM that accurately explains the structural decay is incapable of predicting the long-ranged decay [18, 21, 24, 25], which we refer to as *anomalous* underscreening. Thus, either the RPM is missing a crucial ingredient or the long-ranged decay is an artifact of the experiment. Within this Letter we show that there is a third option.

Underscreening is often categorized by power laws of the form  $\lambda/\lambda_D \sim (\sigma/\lambda_D)^p$ , with ion diameter  $\sigma$ , even though the available data do not cover a single decade. Regular underscreening corresponds to  $p \approx 3/2$  while  $p \approx 3$  is anomalous. The SFA results suggest that  $\lambda/\lambda_D$  depends uniquely on the dimensionless quantity  $\kappa = \sigma/\lambda_D$ , because data for many different electrolytes and ionic liquids all collapse onto one unique curve [10]. This conclusion, however, is misleading. Figure 1 illustrates the phase diagram of the RPM in (a) dimensional and (b) reduced dimensionless units. Every small circle marks a parameter set  $(c, \lambda_B)$  for which we performed Molecular Dynamics (MD) simulations. The triangles and squares correspond to parameters as used in the SFA experiments for different electrolytes and ionic liquids. Curiously, in reduced units all experimentally probed parameter sets collapse onto one curve in the phase diagram. Thus, it is not surprising that the resulting decay lengths do the same.

Simulation and theoretical studies typically explore underscreening by solely varying the concentration exemplified by the large circles in fig. 1. Conversely, the

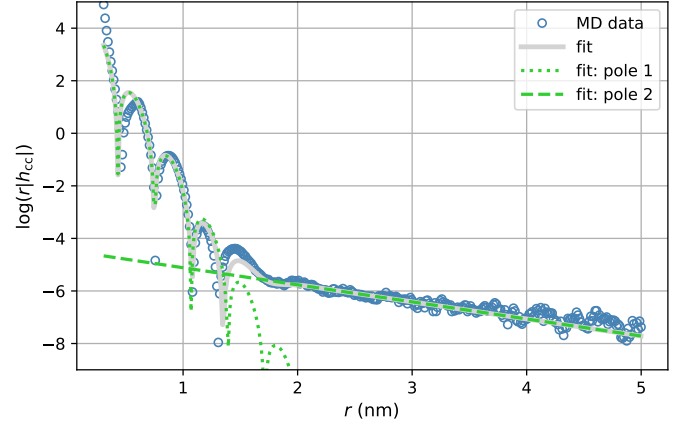


Figure 2. Charge-correlation function  $h_{cc}(r)$  in a representation that shows the decay length as the slope of the graph. This function was sampled by a MD simulation with  $c = 0.1$  mol/L,  $\lambda_B = 5$  nm, and  $\sigma = 0.3$  nm. The pole fits have the analytical form of eq. (1), respectively (see Supplemental Material [46] for further details on the fits).

experimental parameters that exhibit anomalous underscreening at large concentrations predominantly vary in the Bjerrum length. Thus, previous studies only explore limited parts of parameter space. To address this issue, we present MD simulations for a wide range of parameters comprehensively screening the phase diagram as illustrated in fig. 1. In particular, this allows us to extract the decay length as a function of the Bjerrum length for several fixed concentrations. For each set of parameters  $(c, \lambda_B)$  we run MD simulations of the RPM with  $\sigma = 0.3$  nm [further details in the Supplemental Material [46]; the typical size of the cubic simulation box is  $(60 \text{ nm})^3$ ]. Once equilibrated, we sample the radial pair-distribution functions  $g_{\mu\nu}(r)$  and compute the charge correlation  $h_{cc}$ . To extract the principal decay lengths, we fit  $h_{cc}$  to a superposition of decays  $H_i$  [eq. (1)] accounting for up to three poles and a potential branch point – fig. 2 exemplifies the procedure.

The representation  $\log(r|h_{cc}|)$  is chosen in accordance with the known form of the decay in eq. (1) so that the decay length corresponds to the slope of a linear fit. In fig. 2, we find the two previously discussed decay regimes: the structural decay (up to  $r \approx 1.5$  nm) and long-ranged decay ( $r \gtrsim 1.5$  nm). Consistent with the SFA measurements, the long-ranged decay (pole 2) is always found to be monotonic, while the structural decay (pole 1) can also show oscillations depending on the parameters. At very large separations, the decay with the largest decay length dominates. However, in the Supplemental Material [46] we demonstrate that the amplitude  $A_i$  of this dominant contribution may be small such that the signal is buried in statistical noise of the simulations. This complicates the extraction of decay lengths, particularly for large concentrations. Details on the simulations and fitting procedure including the fitted parameters for all charge correlations can be found in [46].

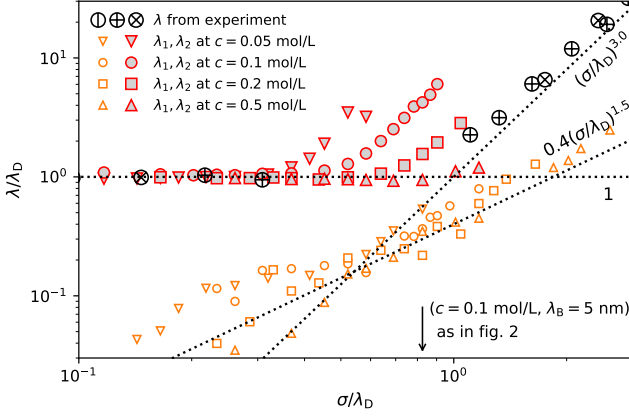


Figure 3. Decay lengths  $\lambda_1$  and  $\lambda_2$  obtained by fitting  $\sum_{i=1}^n H_i(r)$ ,  $n \in \{1, 2, 3\}$  to bulk charge-correlation functions sampled from our MD simulations of the RPM as exemplarily shown in fig. 2.  $\lambda_1$  represents decay lengths of the structural decay and  $\lambda_2$  represents decay lengths of the long-ranged monotonic decay (compare poles 1 and 2 in fig. 2). Note that in some cases we used a third pole for the fit [46]. We show the decay length  $\lambda$  in relation to the Debye length  $\lambda_D$  against  $\sigma/\lambda_D$  (depending on  $\lambda_B$  and  $c$ ), as common in the literature on underscreening [11]. For each given concentration, we varied only the Bjerrum length. Large black circles represent data from experiments on an ionic liquid ( $\circ$ ), NaCl in water ( $+$ ), and [C4C1Pyr][NTf2] in propylene carbonate ( $\times$ ) [5]. Dotted lines depict power laws as noted.

In fig. 3, we present the measured decay lengths that we obtained from our MD simulations at fixed concentration  $c = 0.05/0.1/0.2/0.5$  mol/L, respectively (results for all parameter pairs presented in fig. 1 are shown in the Supplemental Material [46]). Our broad exploration of the phase diagram reveals that there is no unique relationship in reduced parameters. The decay length generally depends on salt concentration and Bjerrum length, independently. If we increase the Bjerrum length at fixed concentration, we find  $\lambda_2$  being the Debye length at small  $\sigma/\lambda_D$  but approximately following a power law  $\lambda_2 \sim (\sigma/\lambda_D)^3$  at larger  $\sigma/\lambda_D$ , as observed in the experiments for dense electrolytes. Each  $\lambda_2$  is accompanied by a much shorter decay length  $\lambda_1$  that describes structural screening. All structural decay lengths  $\lambda_1$  approximately follow a power law  $\lambda_1 \sim (\sigma/\lambda_D)^{1.5}$ , as demonstrated in fig. 3.

The curves of  $\lambda_2$  at fixed concentration that show anomalous underscreening shift to the right in fig. 3 with increasing concentration. At the same time, the amplitude of the decay  $H_2$  from eq. (1) decreases with increasing concentration. At high concentrations, the decay  $H_2(r)$  drops below the numerical resolution of our MD simulation (see [46] for further details). For reference, we also show experimental results for different ionic liquids and electrolytes in fig. 3. Varying the concentration, we only find regular underscreening in the dense regime (data not shown). The extracted decay lengths approxi-

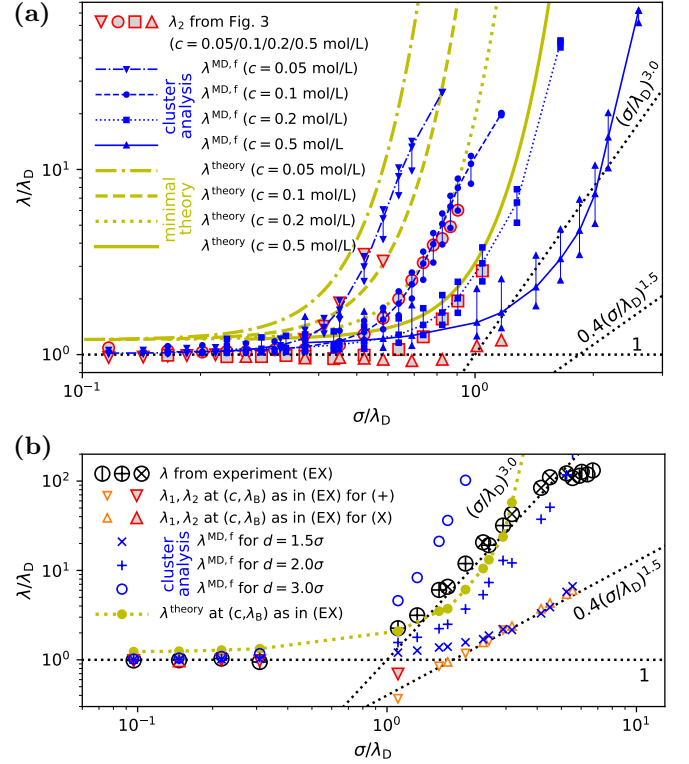


Figure 4. Decay lengths represented as in fig. 3. (a) Symbols without lines show decay lengths of anomalous underscreening ( $\lambda_2$  in fig. 3) as obtained by fitting the charge-correlation functions from our MD simulations of the RPM. Triplets of vertically arranged blue symbols show decay lengths  $\lambda^{\text{MD},f}$  induced by free ions for different connectivity lengths  $d = 1.5\sigma$ ,  $d = 2\sigma$ ,  $d = 3\sigma$  (from top to bottom) in the cluster search algorithm. Yellow lines show the prediction  $\lambda^{\text{theory}}$  of our minimal theory. (b) Directly measured  $\lambda_1$  and  $\lambda_2$  obtained by fitting the charge-correlation functions sampled from our MD simulations for parameter pairs  $(c, \lambda_B)$  as used in the experiments (EX) of [5]. The experimental data are described in fig. 3 and also listed in the Supplemental Material [46]. Blue symbols show the resulting  $\lambda^{\text{MD},f}$  from our cluster analysis for the same parameters. Yellow symbols (line added for clarity) show the corresponding  $\lambda^{\text{theory}}$  from our minimal theory.

mately follow the power law  $0.4(\sigma/\lambda_D)^{1.5}$  (fig. 3), which is consistent with the literature [24].

In conclusion, there is anomalous underscreening in the RPM but it cannot be observed in simulations for parameters suggested by the experiment.

However, if there is anomalous underscreening in the RPM, theoretical approaches should find it as well. Recently, Cats *et al.* presented a comprehensive comparison between available theoretical results and concluded that classical density functional theory (DFT) is a good approach to describe screening in electrolytes and ionic liquids [24]. Classical DFT accurately predicts the structural decay, i.e., regular underscreening [15, 24, 25, 65]. However, DFT calculations for a fixed concentration  $c = 0.1$  mol/L and varying Bjerrum length do not show anomalous underscreening [46], in contrast to our MD

simulations (fig. 3). The predictions of classical DFT reflect the accuracy of the employed excess free energy functional. It stands to reason that the theory does simply not account for the mechanism that causes anomalous underscreening.

Candidates for missing ingredients in the theoretical description are the subject of ongoing discussions. Theoretical models are frequently criticized for their implicit treatment of solvents that can significantly alter the effective steric and electrostatic interactions between ions. However, anomalous underscreening has been reported experimentally for a variety of very different solvents and even for ionic liquids. Moreover, simulations that explicitly accounted for atomistic solvent did not observe anomalous underscreening [18]. A promising contender is a reduction of the concentration of effective charge carriers, for instance, by the formation of Bjerrum pairs or by defects in dense electrolytes taking over the role of mobile charges [1, 7, 23, 66–74]. To estimate the effective concentration of free charge carriers, we analyze system configurations generated by our MD simulations for cluster formation.

To this end, we assign a connectivity shell of diameter  $d > \sigma$  to all particles in our simulation and consider two particles connected if their respective connectivity shells overlap. The clusters detected in this way either comprise the same number of positive and negative charges, such that their collective contribution to screening is supposedly negligible, or have a finite net charge. Based on our cluster results, we safely assume that the absolute net charge of a cluster is either one elementary charge or zero [46]. In consequence, we define free ions by neglecting all clusters that contain an even number of particles and by replacing each cluster that contains an odd number of particles by one free (nonclustered) ion. With increasing Bjerrum length, the fraction of free ions decreases.

We now assume that only free particles contribute to screening and split the number density  $\rho_s$  of all ions into free and bound parts,  $\rho_s = \rho_f + \rho_b$ . Assuming only the free ions cause Debye screening, the expected decay length is simply the Debye length for the reduced density  $\rho_f$ ,  $\lambda^{\text{MD},f} = 1/\sqrt{8\pi\lambda_B\rho_f}$ . In fig. 4(a), the decay lengths resulting from this cluster analysis on the same simulation data that led to the results of fig. 3 are displayed for different connectivity shell diameters  $d = 1.5\sigma, 2\sigma, 3\sigma$  alongside the directly measured decay length  $\lambda_2$  from fig. 3. Our cluster analysis predicts anomalous underscreening very similar to the direct extraction of decay lengths from simulation in fig. 3. It even predicts anomalous underscreening for data points  $(c, \lambda_B)$  where we could not use the direct fitting method due to insufficient numerical resolution. The cluster analysis also shows anomalous underscreening in fig. 4(b) for the same parameter pairs  $(c, \lambda_B)$  as used in the experiments of [5]. With an adequate choice of connectivity diameter, this prediction even matches the experimentally measured decay lengths. However, while the predicted decay length is rather insensitive to the choice of connectivity diameter  $d$  at low con-

centrations, which is a necessary condition for a meaningful trend as  $d$  itself has no physical footing, at higher concentrations the choice of the connectivity diameter matters, rendering the method inapplicable. A better definition of free and bound ions might be facilitated by machine-learned local structures [71, 74]. Nevertheless, our cluster analysis supports the hypothesis that anomalous underscreening is also present at high concentrations in our MD simulations, but its signal is too small to be distinguished from noise [46].

To supplement our explanation of anomalous underscreening, we present a minimal theory that allows ion pairing, similar to previous approaches [66, 69]. We acknowledge that the general mechanism is presumably “not a question of pair formation, but a more general transient association of ions involving several ions of opposite charge” [13]. Our approach is based on the grand canonical description of an electrolyte of positive and negative point charges in a volume  $V$ , where particles either are free or bound in neutral pairs,  $\beta\Omega^{\text{pair}}/V = 2\rho_f(\log(\rho_f\Lambda_f^3) - 1) + \rho_p(\log(\rho_p\Lambda_p^3) - 1) + F^{\text{es}} - \beta\mu_f\rho_f - \beta\mu_p\rho_p$ . We eliminate the thermal wavelengths by identifying  $\Lambda_s = \Lambda_f = \Lambda_p\sqrt{2}$  and comparing with a system of solely pointlike ions. Using  $3/2k_BT$  and the electrostatic bulk energy density  $F^{\text{es}} = -\lambda_D^{-3}/(12\pi)$  [38] for the inner energy per volume in units of  $k_BT$ , we obtain our final result

$$\beta\frac{\Omega^{\text{pair}}}{V} = 2\rho_f(\log(\rho_f/\rho_s) - 1) + \rho_p\left(\log(\rho_p/(\sqrt{2}^3\rho_s) - 1)\right) - \left(1 - \frac{3}{2}\frac{\rho_f}{\rho_s}\right)\frac{\sqrt{8\pi\lambda_B\rho_s}^3}{12\pi} + \frac{3}{2}\rho_p, \quad (2)$$

as derived in more detail in the Supplemental Material [46]. Setting  $\rho_f = \alpha\rho_s$  and  $\rho_p = (1 - \alpha)\rho_s$  in eq. (2), we obtain  $\Omega^{\text{pair}}(\alpha)$  with  $\alpha \in [0, 1]$  that can be minimized with respect to the fraction  $\alpha$  of free ions while  $\rho_s$  is kept fixed.

As previously, in the cluster analysis of our simulation results, we assume that only free ions contribute to the screening of charges. Accordingly, we use the predicted density  $\rho_f^{\text{theory}}$  of free ions to obtain the decay length  $\lambda^{\text{theory}} = 1/\sqrt{8\pi\lambda_B\rho_f^{\text{theory}}}$  as a function of the total ion concentration  $\rho_s$  and the Bjerrum length  $\lambda_B$ . In fig. 4, we sketch the predictions of this theory of ion pairing in comparison to our results from MD simulations and experimental data. Clearly, our minimal theory predicts an even stronger increase of the decay length than is found in simulations or experiments. While this increase starts at lower  $\sigma/\lambda_D$  than expected [see fig. 4(a)], the theory confirms the shift to larger  $\sigma/\lambda_D$  with increasing ion concentration. In fig. 4(b), the theory reproduces the strong increase of the experimentally reported decay lengths and its position in the plot remarkably well.

In summary, we show that anomalous underscreening, which previously has only been reported experimentally, can also be found in the RPM using MD simulations. Our results demonstrate that the decay length is, in general,

not a unique function of the parameter  $\sigma/\lambda_D$  as suggested by experiments [10], but the experiments probe only a unique line in the phase diagram of the RPM. On top of that, we illustrate that cluster formation induces a strong increase of the screening length, which provides an explanation for anomalous underscreening. We support this explanation, on the one hand, by analyzing clusters in our MD simulations and, on the other hand, by applying a minimal cluster theory of ion pairing which allows ions to form neutral pairs.

Finally, the question remains why some experiments could find anomalous underscreening and others could not. As a possible answer, it has been proposed that the atomic force microscope has by construction a much lower sensitivity than the SFA [1, 75]. Accordingly, the signal of anomalous underscreening might be too small

for some of the experiments, similar to the sensitivity of our MD simulations [46].

## ACKNOWLEDGEMENTS

We thank Patrick Warren, Fabian Glatzel, and Anja Kuhnhold for fruitful discussions. AH and MB acknowledge funding from the German Research Foundation (DFG) through Project No. 406121234. FC acknowledges funding from the German Research Foundation (DFG) through Project No. 457534544. We acknowledge support by the state of Baden-Württemberg through bwHPC and the German Research Foundation (DFG) through Grant No. INST 39/963-1 FUGG (bwForCluster NEMO).

- 
- [1] M. A. Gebbie, M. Valtiner, X. Banquy, E. T. Fox, W. A. Henderson, and J. N. Israelachvili, *Proceedings of the National Academy of Sciences* **110**, 9674 (2013).
  - [2] M. A. Gebbie, H. A. Dobbs, M. Valtiner, and J. N. Israelachvili, *Proceedings of the National Academy of Sciences* **112**, 7432 (2015).
  - [3] H.-W. Cheng, P. Stock, B. Moeremans, T. Baimpos, X. Banquy, F. U. Renner, and M. Valtiner, *Advanced Materials Interfaces* **2**, 1500159 (2015).
  - [4] R. M. Espinosa-Marzal, A. Arcifa, A. Rossi, and N. D. Spencer, *The Journal of Physical Chemistry Letters* **5**, 179 (2014).
  - [5] A. M. Smith, A. A. Lee, and S. P. Perkin, *The Journal of Physical Chemistry Letters* **7**, 2157 (2016).
  - [6] N. Hjälmarsson, R. Atkin, and M. W. Rutland, *Chemical Communications* **53**, 647 (2017).
  - [7] A. M. Smith, P. Maroni, G. Trefalt, and M. Borkovec, *The Journal of Physical Chemistry B* **123**, 1733 (2019).
  - [8] P. Gaddam and W. Ducker, *Langmuir* **35**, 5719 (2019).
  - [9] M. A. Gebbie, A. M. Smith, H. A. Dobbs, A. A. Lee, G. G. Warr, X. Banquy, M. Valtiner, M. W. Rutland, J. N. Israelachvili, S. Perkin, and R. Atkin, *Chemical Communications* **53**, 1214 (2017).
  - [10] A. A. Lee, C. S. Perez-Martinez, A. M. Smith, and S. Perkin, *Physical Review Letters* **119**, 026002 (2017).
  - [11] A. A. Lee, C. S. Perez-Martinez, A. M. Smith, and S. Perkin, *Faraday Discussions* **199**, 239 (2017).
  - [12] Z. A. H. Goodwin and A. A. Kornyshev, *Electrochemistry Communications* **82**, 129 (2017).
  - [13] R. Kjellander, *The Journal of Chemical Physics* **148**, 193701 (2018).
  - [14] B. Rotenberg, O. Bernard, and J.-P. Hansen, *Journal of Physics: Condensed Matter* **30**, 054005 (2018).
  - [15] F. Coupette, A. A. Lee, and A. Härtel, *Physical Review Letters* **121**, 075501 (2018).
  - [16] R. M. Adar, S. A. Safran, H. Diamant, and D. Andelman, *Physical Review E* **100**, 042615 (2019).
  - [17] S. W. Coles, C. Park, R. Nikam, M. Kanduč, J. Dzubiella, and B. Rotenberg, *The Journal of Physical Chemistry B* **124**, 1778 (2020).
  - [18] J. Zeman, S. Kondrat, and C. Holm, *Chemical Communications* **56**, 15635 (2020).
  - [19] N. Anousheh, F. J. Solis, and V. Jadhao, *AIP Advances* **10**, 125312 (2020).
  - [20] R. Kjellander, *Physical Chemistry Chemical Physics* **22**, 23952 (2020).
  - [21] J. Zeman, S. Kondrat, and C. Holm, *The Journal of Chemical Physics* **155**, 204501 (2021).
  - [22] A. Ciach and O. Patsahan, *Journal of Physics: Condensed Matter* **33**, 37LT01 (2021).
  - [23] E. Krucker-Velasquez and J. W. Swan, *The Journal of Chemical Physics* **155**, 134903 (2021).
  - [24] P. Cats, R. Evans, A. Härtel, and R. van Roij, *The Journal of Chemical Physics* **154**, 124504 (2021).
  - [25] S. Kumar, P. Cats, M. B. Alotaibi, S. C. Ayirala, A. A. Yousef, R. van Roij, I. Siretanu, and F. Mugele, *Journal of Colloid and Interface Science* **622**, 819 (2022).
  - [26] S. Schön and R. von Klitzing, *Beilstein Journal of Nanotechnology* **9**, 1095 (2018).
  - [27] P. Simon and Y. Gogotsi, *Nature Materials* **7**, 845 (2008).
  - [28] D. Brogioli, *Physical Review Letters* **103**, 058501 (2009).
  - [29] A. Härtel, M. Janssen, D. Weingarth, V. Presser, and R. van Roij, *Energy & Environmental Science* **8**, 2396 (2015).
  - [30] S. Porada, R. Zhao, A. van der Wal, V. Presser, and P. Biesheuvel, *Progress in Materials Science* **58**, 1388 (2013).
  - [31] E. J. W. Verwey, J. T. G. Overbeek, and K. van Nes, *Theory of the Stability of Lyophobic Colloids: The Interaction of Sol Particles Having an Electric Double Layer* (Elsevier Publishing Company, 1948).
  - [32] B. Derjaguin and L. Landau, *Progress in Surface Science* **43**, 30 (1993).
  - [33] Y. Li, M. Girard, M. Shen, J. A. Millan, and M. O. de la Cruz, *Proceedings of the National Academy of Sciences* **114**, 11838 (2017).
  - [34] A. A. Kornyshev, D. J. Lee, S. Leikin, and A. Wynveen, *Reviews of Modern Physics* **79**, 943 (2007).
  - [35] J. R. Espinosa, M. Galván, A. S. Quiñones, J. L. Ayala, and S. M. Durón, *Sensors (Basel)* **19**, 3956 (2019).
  - [36] M. Shapiro, K. Homma, S. Villarreal, C.-P. Richter, and F. Bezanilla, *Nature Communications* **3**, 736 (2012).
  - [37] A. C. L. de Lichtervelde, J. P. de Souza, and M. Z. Bazant, *Physical Review E* **101**, 022406 (2020).

- [38] P. Debye and E. Hückel, *Physikalische Zeitschrift* **24**, 185 (1923).
- [39] A. M. Smith, A. A. Lee, and S. Perkin, *Physical Review Letters* **118**, 096002 (2017).
- [40] P. Attard, C. P. Ursenbach, and G. N. Patey, *Physical Review A* **45**, 7621 (1992).
- [41] R. Kjellander and D. J. Mitchell, *Chemical Physics Letters* **200**, 76 (1992).
- [42] R. Evans, J. R. Henderson, D. C. Hoyle, A. O. Parry, and Z. A. Sabeur, *Molecular Physics* **80**, 755 (1993).
- [43] R. Evans, R. J. F. Leote de Carvalho, J. R. Henderson, and D. C. Hoyle, *The Journal of Chemical Physics* **100**, 591 (1994).
- [44] J. Ennis, R. Kjellander, and D. J. Mitchell, *The Journal of Chemical Physics* **102**, 975 (1995).
- [45] J. Ulander and R. Kjellander, *The Journal of Chemical Physics* **114**, 4893 (2001).
- [46] See Supplemental Material at <http://link.aps.org/supplemental/10.1103/PhysRevLett.130.108202> for details on the simulations, the fitting of decay lengths, and the derivation of the minimal cluster theory, which includes [47–60].
- [47] J.-P. Hansen and I. R. McDonald, *Theory of Simple Liquids*, 4th ed. (Elsevier, Oxford, 2013).
- [48] F. Weik, R. Weeber, K. Szuttor, K. Breitsprecher, J. de Graaf, M. Kuron, J. Landsgesell, H. Menke, D. Sean, and C. Holm, *The European Physical Journal Special Topics* **227**, 1789 (2019).
- [49] H. C. Andersen, J. D. Weeks, and D. Chandler, *Physical Review A* **4**, 1597 (1971).
- [50] J. D. Weeks, D. Chandler, and H. C. Andersen, *The Journal of Chemical Physics* **54**, 5237 (1971).
- [51] R. W. Hockney and J. W. Eastwood, *Computer simulation using particles* (IOP, London, 1988).
- [52] P. González-Mozuelos, G. I. Guerrero-García, and M. Olvera de la Cruz, *The Journal of Chemical Physics* **139**, 064709 (2013).
- [53] R. Evans, *Advances in Physics* **28**, 143 (1979).
- [54] A. Härtel, *Journal of Physics: Condensed Matter* **29**, 423002 (2017).
- [55] R. Roth and D. Gillespie, *Journal of Physics: Condensed Matter* **28**, 244006 (2016).
- [56] Y. Rosenfeld, *Physical Review Letters* **63**, 980 (1989).
- [57] R. Roth, *Journal of Physics: Condensed Matter* **22**, 063102 (2010).
- [58] H. Hansen-Goos and R. Roth, *Journal of Physics: Condensed Matter* **18**, 8413 (2006).
- [59] J. K. Percus, *Physical Review Letters* **8**, 462 (1962).
- [60] H. L. Frisch and J. L. Lebowitz, *The Equilibrium Theory of Classical Fluids: a Lecture Note and Reprint volume* (WA Benjamin, New York, 1964).
- [61] J. G. Kirkwood, *The Journal of Chemical Physics* **7**, 919 (1939).
- [62] R. J. F. Leote de Carvalho and R. Evans, *Molecular Physics* **83**, 619 (1994).
- [63] G. Orkoulas and A. Z. Panagiotopoulos, *The Journal of Chemical Physics* **101**, 1452 (1994).
- [64] A.-P. Hynninen, M. E. Leunissen, A. van Blaaderen, and M. Dijkstra, *Physical Review Letters* **96**, 018303 (2006).
- [65] M. Bültmann and A. Härtel, *Journal of Physics: Condensed Matter* **34**, 235101 (2022).
- [66] J. Zwanikken and R. van Roij, *Journal of Physics: Condensed Matter* **21**, 424102 (2009).
- [67] F. W. Richey, B. Dyatkin, Y. Gogotsi, and Y. A. Elabd, *Journal of the American Chemical Society* **135**, 12818 (2013).
- [68] M. A. Gebbie, M. Valtiner, X. Banquy, W. A. Henderson, and J. N. Israelachvili, *Proceedings of the National Academy of Sciences* **110**, E4122 (2013).
- [69] R. M. Adar, T. Markovich, and D. Andelman, *The Journal of Chemical Physics* **146**, 194904 (2017).
- [70] G. Feng, M. Chen, S. Bi, Z. A. H. Goodwin, E. B. Postnikov, N. Brilliantov, M. Urbakh, and A. A. Kornyshev, *Physical Review X* **9**, 021024 (2019).
- [71] P. Jones, F. Coupette, A. Härtel, and A. A. Lee, *The Journal of Chemical Physics* **154**, 134902 (2021).
- [72] J. M. Dean, S. W. Coles, W. R. Saunders, A. R. McCluskey, M. J. Wolf, A. B. Walker, and B. J. Morgan, *Physical Review Letters* **127**, 135502 (2021).
- [73] Z. A. H. G. Goodwin, M. McEldrew, P. de Souza, M. Z. Bazant, and A. A. Kornyshev, *The Journal of Chemical Physics* **157**, 094106 (2022).
- [74] P. K. Jones, K. D. Fong, K. A. Persson, and A. A. Lee, “Inferring global dynamics from local structure in liquid electrolytes,” (2022), arXiv:2208.03182 [cond-mat.soft].
- [75] T. Baimpos, B. R. Shrestha, S. Raman, and M. Valtiner, *Langmuir* **30**, 4322 (2014).

# Supplemental Material for: Anomalous Underscreening in the Restricted Primitive Model

Andreas Härtel,<sup>1,\*</sup> Moritz Bültmann,<sup>1</sup> and Fabian Coupette<sup>1</sup>

<sup>1</sup>*Institute of Physics, University of Freiburg, Hermann-Herder-Straße 3, 79104 Freiburg, Germany*

(Published as Supplemental Material for: Physical Review Letters **130**, 108202 (2023), DOI: 10.1103/PhysRevLett.130.108202)

In this supplemental material for our article “Anomalous Underscreening in the Restricted Primitive Model” we present details on the (I.) minimal theory of ion pairing we used, on the (II.) Molecular Dynamics simulations we performed, on the (III.) cluster analysis of our simulation results, on the (IV.) theoretical foundations of decay lengths, and on the extraction of decay lengths from (V.) fitting of charge-correlation functions. We further show (VI.) additional results from density functional theory and list in table S2 the parameters and the corresponding measured decay lengths as reported for experimental measurements in the supporting information of [S1].

## I. MINIMAL THEORY OF ION PAIRING

We consider a system of ideal positive and negative charges in a volume  $V$  at temperature  $T$ . Each species has a number density  $\rho_s$ . With three degrees of freedom per particle, the internal energy  $U$  of this system is

$$\beta \frac{U}{V} = \frac{3}{2} 2\rho_s + F^{\text{es}}, \quad (\text{S1})$$

with the bulk electrostatic energy  $F^{\text{es}} = -\sqrt{8\pi\lambda_B\rho_s^3}/(12\pi)$  as derived by Debye and Hückel [S2] and the inverse temperature  $\beta = 1/k_B T$  setting the thermal energy. As in the main article,  $k_B$  is Boltzmann’s constant and  $\lambda_B$  the Bjerrum length. The chemical potential follows from eq. (S1) with

$$\beta\mu_s^{\text{TD}} = \left( \frac{\partial \beta \frac{U}{V}}{\partial \rho_s} \right)_{S,V} = 3 + \frac{3}{2} F^{\text{es}} \frac{1}{\rho_s}, \quad (\text{S2})$$

where the entropy  $S$  is a thermodynamic state variable. From another perspective, the grand potential  $\Omega$  of the system reads

$$\beta \frac{\Omega}{V} = 2\rho_s (\log(\rho_s \Lambda_s^3) - 1) + F^{\text{es}} - \beta\mu_s \rho_s \quad (\text{S3})$$

with the thermal de Broglie wavelength  $\Lambda_s$ . As in classical density functional theory (DFT) [S3], the variational principle

$$\frac{\delta \beta \frac{\Omega}{V}}{\delta \rho_s} = 2 \log(\rho_s \Lambda_s^3) + \frac{3}{2} F^{\text{es}} \frac{1}{\rho_s} - \beta\mu_s \stackrel{!}{=} 0 \quad (\text{S4})$$

holds for the true physical system in equilibrium.

As we aim for a description of free and paired ions, we now consider three species, namely positive and negative free ions with number density  $\rho_f$  and neutral pairs of ions with number density  $\rho_p$ . The total number of ions

is conserved by  $\rho_s = \rho_f + \rho_p$ . The grand potential of this system is given by

$$\begin{aligned} \beta \frac{\Omega^{\text{pair}}}{V} = & 2\rho_f (\log(\rho_f \Lambda_f^3) - 1) + \rho_p (\log(\rho_p \Lambda_p^3) - 1) \\ & + F^{\text{es}} - \beta\mu_f \rho_f - \beta\mu_p \rho_p. \end{aligned} \quad (\text{S5})$$

Free ions have the same thermal wavelength as the salt but a pair has twice the mass of a free ion leading to  $\Lambda_s = \Lambda_f = \Lambda_p \sqrt{2}$ . Furthermore, the internal energy of the system does not change with changing the number of pairs, thus, we identify  $\mu_f = \mu_s$  and  $\mu_p = 0$ . Combining eqs. (S4) and (S5) we can eliminate the thermal wavelengths. In a last step we identify  $\mu_s = \mu_s^{\text{TD}}$  and insert eq. (S2) yielding our final result

$$\begin{aligned} \beta \frac{\Omega^{\text{pair}}}{V} = & 2\rho_f (\log(\rho_f/\rho_s) - 1) + \rho_p (\log(\rho_p/(\sqrt{2}^3 \rho_s) - 1) \\ & + \left(1 - \frac{3}{2} \frac{\rho_f}{\rho_s}\right) F^{\text{es}} + \frac{3}{2} \rho_p. \end{aligned} \quad (\text{S6})$$

Setting  $\rho_f = \alpha \rho_s$  and  $\rho_p = (1 - \alpha) \rho_s$  in eq. (S6), we obtain  $\Omega^{\text{pair}}(\alpha)$  with  $\alpha \in [0, 1]$  that can be minimized with respect to the fraction  $\alpha$  of free ions while  $\rho_s$  is kept fixed.

## II. SIMULATION DETAILS

We consider the RPM of charged hard spheres with ion diameter  $\sigma$  and valencies  $Z_{\pm} = \pm 1$ . The bulk system at temperature  $T = 293.41$  K has a thermal energy  $\beta^{-1} = k_B T$  with Boltzmann’s constant  $k_B$ . As in previous work [S4], we perform extensive Molecular Dynamics (MD) simulations using the ESPResSo package [S5]. Namely, we performed MD simulations of the RPM with different ion concentrations  $c$  and Bjerrum lengths  $\lambda_B$ , while in most cases the ion diameter was set to  $\sigma = 0.3$  nm.

In our MD simulation we measure energy in  $k_B T$  and distances in nm which in combination with the mass  $3 \cdot 10^{-23}$  g of each of all the particles in the system defines the characteristic time scale of 2.699 ps. We model the

---

\* andreas.haertel@physik.uni-freiburg.de



hard steric repulsion between ions by a Weeks-Chandler-Anderson potential [S6, S7]

$$u_{\text{WCA}}(r) = \begin{cases} 4\gamma \left( \left( \frac{\sigma_{\text{LJ}}}{r} \right)^{12} - \left( \frac{\sigma_{\text{LJ}}}{r} \right)^6 + \frac{1}{4} \right) & r < \sigma \\ 0 & r \geq \sigma \end{cases} \quad (\text{S7})$$

with  $\gamma = 5 \cdot 10^3 k_{\text{B}}T$  and  $\sigma_{\text{LJ}} = 2^{-1/6}\sigma$  such that the potential is purely repulsive and its derivative is continuous at  $\sigma$ . To compute the electrostatic forces between ions, we use the P3M method, a sophisticated Ewald summation technique implemented in ESPResSo [S5, S8]. The system is coupled to a heat bath via a Langevin thermostat. We simulate a bulk system by calculating ion trajectories in an almost cubic simulation box of volume  $L_x \times L_y \times L_z$  with periodic boundary conditions. After setting  $L_x = L_y = L_z$  and the concentration  $c$  of positive and negative particles, respectively, we slightly have to adjust  $L_x$  and  $L_y$  such that an integer number of particles fits into the simulation box at the chosen  $L_z$  and  $c$ . Note that instead of the concentration, equivalently often the number density  $\rho_s$  of each ion species is used.

Each simulation is initiated by a random configuration that is relaxed by slowly increasing the repulsive inter-particle potential  $u_{\text{WCA}}$ . After switching on the additional electrostatic particle interactions, the system is evolved until the energy of the system fluctuates on a stable level. Then we start sampling radial pair-distribution functions  $g_{\mu\nu}(r)$  between particles of species  $\mu$  and  $\nu$ , respectively using a histogram featuring 400 equidistant bins covering the separation interval  $r \in [0, 5]$  nm in order to achieve a high resolution. Between two configurations analyzed in this way we perform 1000 integration steps to decorrelate the respective system snapshots. To achieve better statistics we perform several independent simulation runs of the same system in parallel. In table S3 we list concentration  $c$ , Bjerrum length  $\lambda_{\text{B}}$ , ion diameter  $\sigma$ , system size  $L_z$ , and the total number of configurations  $N_{\text{g}}$  used for sampling a radial pair-distribution function for all simulations analyzed. A typical system size is  $L_z = 60$  nm and the number of configurations that the radial distribution functions are averaged over ranges from  $10^3$  up to  $10^6$ , depending on system size and the concentration. The number of particles that we used for a system size of  $L = 60$  nm is summarized in table S1 for concentrations  $c = 0.05$  mol/L, 0.1 mol/L, 0.2 mol/L, 0.5 mol/L and can be extracted for all simulated systems from the parameters listed in table S3.

Table S1. Size  $L_x \times L_y \times L_z$  of the simulation box and number  $N_{\pm}$  of positive and negative ions, respectively, at a given concentration  $c$ .  $N_+ = N_-$  ensures overall charge neutrality.

$c$ (mol/L)	$L_x = L_y$ (nm)	$L_z$ (nm)	$N_{\pm}$
0.05	$\approx 60.00111$	60	6504
0.1	$\approx 60.00111$	60	13008
0.2	$\approx 60.00111$	60	26016
0.5	$\approx 60.00018$	60	65038

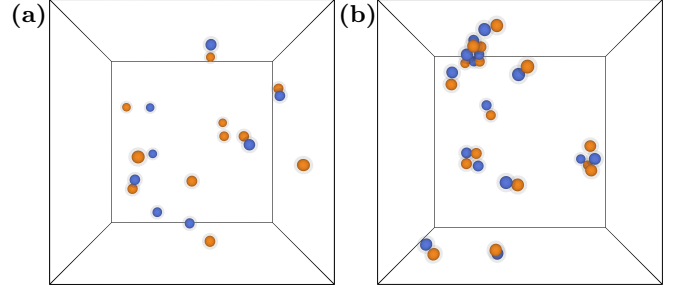


Figure S1. Snippets from particle configurations obtained from MD simulations at  $c = 0.1$  mol/L and (a)  $\lambda_{\text{B}} = 0.7$  nm and (b)  $\lambda_{\text{B}} = 5$  nm. The particle diameter is  $\sigma = 0.3$  nm and the connectivity diameter is  $d = 1.5\sigma$ . Each snippet has the size  $6 \times 6 \times 5$  nm<sup>3</sup>, where the depth is 5 nm.

### III. CLUSTER ANALYSIS OF THE SIMULATION RESULTS

For increasing Bjerrum length we observed a clustering of ions in our MD simulation results. An example is illustrated in fig. S1 for a system at  $c = 0.1$  mol/L. The figure shows two identically sized snippets from systems simulated at different Bjerrum lengths (a)  $\lambda_{\text{B}} = 0.7$  nm and (b)  $\lambda_{\text{B}} = 5$  nm. At higher Bjerrum length we observe a multitude of clusters with even number of ions. Typically, the charge of all ions in such an even cluster sums up to zero, as we will demonstrate in the following.

For a more detailed analysis we performed a cluster analysis on some of the particle configurations that we used to sample the pair-distribution functions. In this cluster analysis we identified particles in a configuration as connected or clustered if their distance to neighbouring particles was less than a connectivity distance  $d > \sigma$ . All particles that are connected with each other form a cluster. The size of a cluster is given by the number  $N_c$  of particles forming it.

An overview over the detected clusters and their average charge is presented in figs. S2 to S5, where the figures show results for the concentrations  $c = 0.05$  mol/L, 0.1 mol/L, 0.2 mol/L, and 0.5 mol/L, respectively. Each figure, again, contains three panels that show results for different Bjerrum lengths as indicated above each panel. In each panel, the number of particles in a cluster  $N_c$  is given on the  $x$ -axis. For each cluster size  $N_c$ , again, data is shown for three different connectivity distances  $d$ , sorted from left to right and distinguished by three different symbols for the fraction of ions as indicated in each panel. If no symbol is shown, no clusters of the respective size  $N_c$  have been found in the analyzed configurations for the given connectivity distance  $d$ .

The figs. S2 to S5 show the average absolute charge on clusters of a given size  $N_c$  by red bars with error bars that indicate the standard deviation (left  $y$ -axis). In addition, blue symbols indicate the fraction  $n_{N_c}$  of ions in the system that are clustered in clusters of the respective size  $N_c$ . As the data shows, a small fraction  $n_{N_c}$



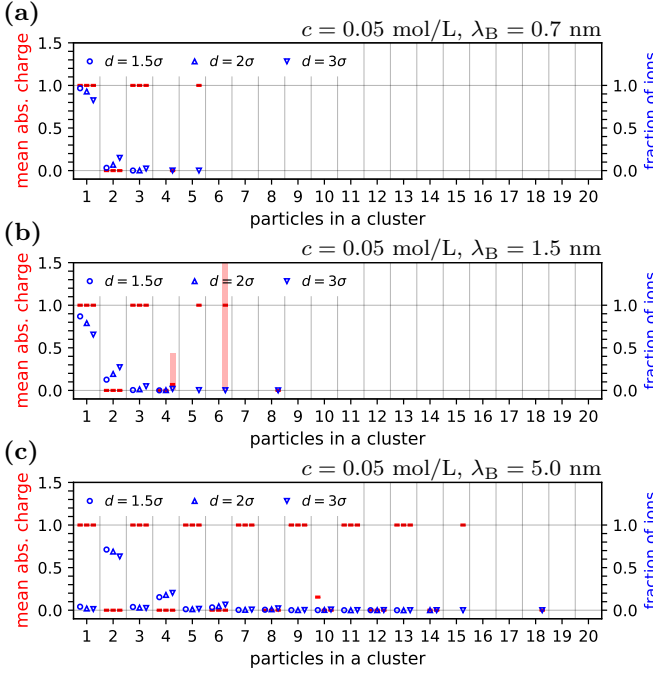


Figure S2. Mean absolute charge (in elementary charges  $e$ ) of clusters that contain  $N_c$  particles (red bars, left axis) and fraction of ions in all cluster of the respective size with respect to the number of ions in the system (blue symbols, right axis). The data depends on the connectivity length  $d$ , thus, on the definition of a cluster. For each cluster size  $N_c$  with a respective number of particles in a cluster three values for  $d = 1.5\sigma$ ,  $2\sigma$ ,  $3\sigma$  are shown. Averages were taken for all clusters found in 10 spatial configuration snapshots of a simulation with concentration  $c = 0.05$  mol/L and Bjerrum length (a)  $\lambda_B = 0.7$  nm, (b)  $1.5$  nm, and (c)  $5.0$  nm. Bars indicate the standard deviation from the absolute mean charge. If no clusters of a certain size were found, no data points are shown.

comes with a huge standard deviation due to a small total number of available clusters of the respective size, for instance for a cluster of size  $N_c = 6$  in panel (b) of fig. S2 ( $c = 0.05$  mol/L,  $\lambda_B = 1.5$  nm,  $d = 3\sigma$ ). The figures further demonstrate that the standard deviation of the average charge is larger for larger concentrations, which is expected for dense systems where the definition of a cluster is problematic.

The analysis in figs. S2 to S5 shows that most clusters carry a net charge of 0 or  $\pm 1$  elementary charges  $e$ . This holds in particular for low concentrations as well as for large Bjerrum lengths. Based on this finding, we simplify our cluster analysis and assume even clusters (clusters of even size) to be overall charge neutral and odd clusters (clusters of odd size) to carry on average only one positive or one negative net elementary charge  $e$ . Consequently, we also assume that even clusters do not contribute to global screening at all and odd clusters contribute to global screening as if they were free (not clustered) ions.

In conclusion we define the number of odd clusters (not

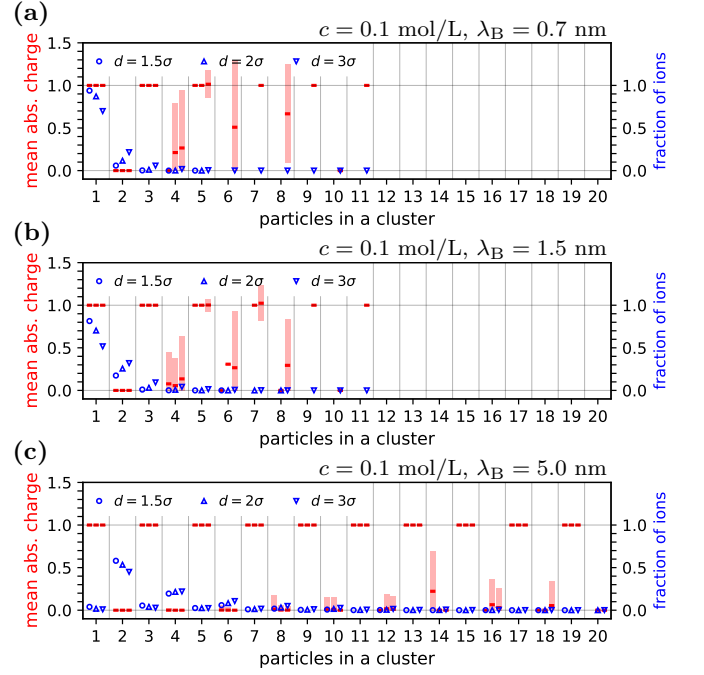


Figure S3. Mean absolute charge of clusters (in elementary charges  $e$ ) and fraction of all ions in a cluster as described in the caption of fig. S2 for systems of concentration  $c = 0.1$  mol/L and Bjerrum length (a)  $\lambda_B = 0.7$  nm, (b)  $1.5$  nm, and (c)  $5.0$  nm.

of the ions) as the number of free ions that still contribute to global screening. This definition includes all ions that are not clustered as well as the clusters that contain an odd number of ions such that the net charge of the cluster is that of a single ion. With increasing Bjerrum length the fraction of free ions decreases, which is shown in fig. S6. This result depends on the connectivity diameter  $d$  that defines the distribution of clusters.

With increasing concentration, the cluster definition becomes problematic, because the choice of the connectivity distance determines the cluster size distribution. As the concentration is increased, the average number of particles in a cluster rises up to the point at which the entire system is spanned by one single cluster.

#### IV. DECAY LENGTH THEORY

At sufficiently large separations  $r$ , the charge-correlation function  $h_{cc}(r)$  decays proportional to  $\exp(-r/\lambda)/r$  [S9–S13] defining the screening length  $\lambda$ . More precisely, in liquid-state theory the species dependent pair-correlation functions are related to the so-called direct correlation functions via the Ornstein-Zernike equation [S3] which yields an algebraic matrix equation in Fourier space. In the RPM the eigenvalues of this matrix correspond to charge- and density-correlation function, respectively. Using contour integration, the inverse Fourier transform of the charge-correlation function

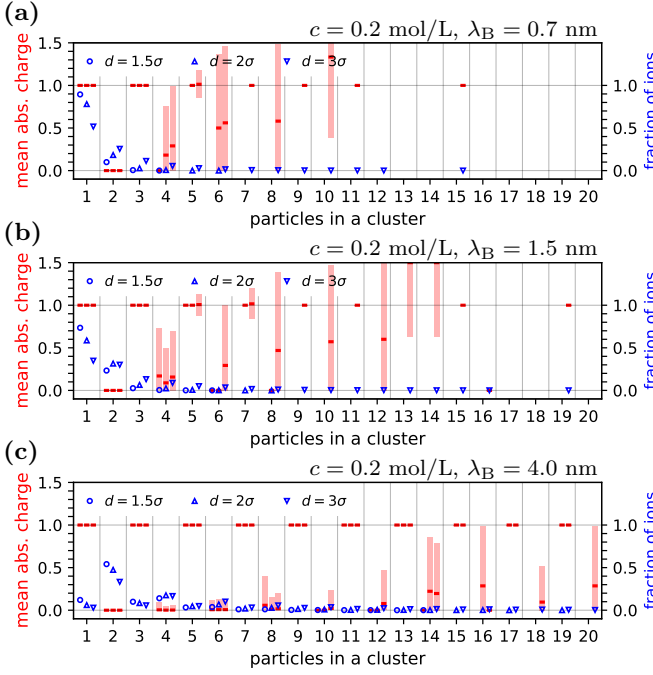


Figure S4. Mean absolute charge of clusters (in elementary charges  $e$ ) and fraction of all ions in a cluster as described in the caption of fig. S2 for systems of concentration  $c = 0.2$  mol/L and Bjerrum length (a)  $\lambda_B = 0.7$  nm, (b)  $1.5$  nm, and (c)  $4.0$  nm; in (c) we show data for  $\lambda_B = 4$  nm instead of  $5$  nm.

can be expressed formally as a sum indexed by the set  $Q_{cc}$  of all complex singularities of a rational function in the Fourier transforms of the direct correlation functions (see [S14] for a brief description).

Each simple pole  $q_i \in Q_{cc}$  now adds a contribution  $P_i(r)$  to the charge-correlation function  $h_{cc}(r)$ , which is of the form

$$P_i(r) = A_i \exp(-r/\lambda_i) \cos(\omega_i r + \tau_i)/r \quad (S8)$$

with decay length  $\lambda_i$ , amplitude  $A_i$ , and  $\omega_i$  and  $\tau_i$  describing potential oscillations. In the limit of large separations,  $r \rightarrow \infty$ , all contributions become negligible compared to the term  $P_i$  with the largest decay length  $\lambda_i$ . This asymptotically dominant decay length of the charge-correlation function is the electrostatic screening length. In addition to the poles, a branch-point singularity can appear that leads to a slightly different decay contribution [S15, S16]

$$B_i(r) = A_i \exp(-r/\lambda_i) \cos(\omega_i r + \tau_i)/r^2. \quad (S9)$$

Notice, that analogous definitions can be made for density correlations  $h_{dd}$  (also labeled particle-particle correlations) that lead to a similar decay length  $\lambda_{dd}$  which may exceed the electrostatic screening length. In the RPM, the longer of the two decay lengths dominates the decay of all pair-distribution functions  $g_{\mu\nu}$  at long separations [S14]. This gives rise to a potential crossover from charge-dominated to density-dominated decay [S14]. Yet, charge

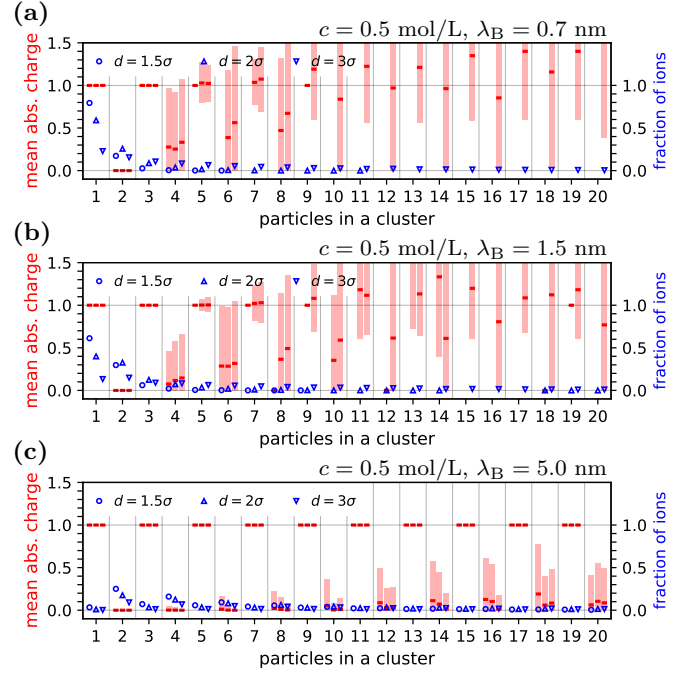


Figure S5. Mean absolute charge of clusters (in elementary charges  $e$ ) and fraction of all ions in a cluster as described in the caption of fig. S2 for systems of concentration  $c = 0.5$  mol/L and Bjerrum length (a)  $\lambda_B = 0.7$  nm, (b)  $1.5$  nm, and (c)  $5.0$  nm.

and density correlations are related to the total correlation functions  $h_{\mu\nu} := g_{\mu\nu} - 1$  via

$$h_{cc} = \frac{1}{2} \sum_{\mu} \sum_{\nu} Z_{\mu} Z_{\nu} h_{\mu\nu}, \quad (S10)$$

$$h_{dd} = \frac{1}{2} \sum_{\mu} \sum_{\nu} h_{\mu\nu}. \quad (S11)$$

Charge inversion symmetry implies  $h_{++} = h_{--}$  and  $h_{+-} = h_{-+}$  such that the above equations reduce to  $h_{cc} = h_{++} - h_{+-}$  and  $h_{dd} = h_{++} + h_{+-}$  in the RPM. Thus, we can specifically compute  $h_{cc} = g_{++} - g_{+-}$ , the dominant decay of which always corresponds to the electrostatic screening length. Moreover, as long as the ion diameter is not significantly larger than the Bjerrum length, the asymptotic decay in the RPM is charge-driven.

## V. FITTING OF CHARGE-CORRELATION FUNCTIONS

To extract decay lengths from our MD simulations, we perform fits to the sampled charge-correlation functions. This method is sufficient for our purposes, but we acknowledge the existence of more advanced methods of extracting asymptotic decay lengths [S16, S17]. Depending on the complexity of the simulation result, we use up

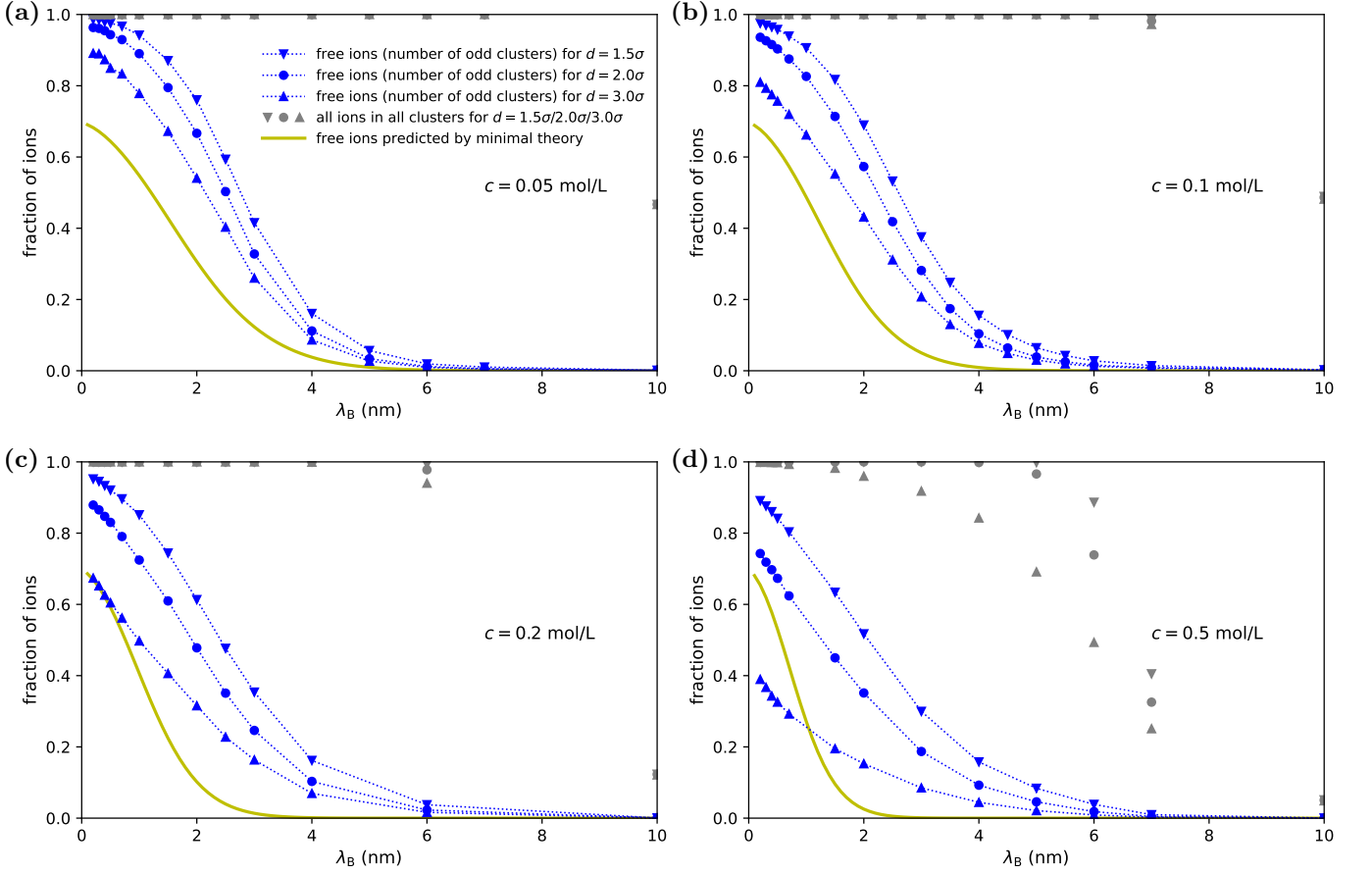


Figure S6. Fraction of free ions in a system at concentration (a)  $c = 0.05$  mol/L, (b)  $0.1$  mol/L, (c)  $0.2$  mol/L, and (d)  $0.5$  mol/L and Bjerrum length  $\lambda_B$ . Dotted lines guide the eyes. Gray symbols without dotted lines show the total fraction of particles in all clusters up to size  $N_c = 40$ . The fraction of ions depends on the connectivity length  $d$ , thus, on the definition of a cluster. For each cluster size with  $N_c$  particles in a cluster three values for  $d = 1.5\sigma, 2\sigma, 3\sigma$  are shown. Averages were taken for all clusters found in 10 spatial configuration snapshots of a simulation at respective parameters. The yellow solid line shows the prediction from the minimal theory of ion pairing.

to three pole contributions  $P_i$  from eq. (S8) and up to one branch contribution  $B_i$  from eq. (S9) to fit the sampled charge-correlation function. The range which we can subject to the fit is limited by numerical noise and is chosen manually because the point at which the correlation has decayed to the level of statistical noise varies heavily with the system parameters. All sampled charge-correlation functions, the resulting fits, and their decomposition into contributions  $P_i(r)$  or  $B_i(r)$  are shown in figs. S8 to S20. The corresponding fitting parameters are listed in table S3 alongside the reference to the figure and panel displaying the fit. Each plot of the figures shows  $\log(r|h_{cc}(r)|)$ . In this representation the slope of the graph encodes the decay length of the corresponding contribution  $P_i$  in eq. (S8).

In fig. S12(bd) we exemplify the procedure. The fit slightly deviates from the signal in the region where the decay changes between different regimes, i.e., from pole 1 to pole 2. Close to particle contact (at  $r = \sigma$ ), the argument of the exponential of each contribution is too small to scale-separate the longest decay length from sub-

dominant contributions of other poles which also causes deviations. At larger separations the signal of our charge-correlation function becomes noisy hinging at the numerical limitations of our approach.

## VI. ADDITIONAL RESULTS FROM DENSITY FUNCTIONAL THEORY

To complement our results, we additionally calculate charge-correlation functions using classical density functional theory (DFT). In DFT, the thermodynamic grand potential is expressed as a functional of the one-body number density profiles  $\rho_\nu(\vec{r})$  of all species  $\nu$  that depend on the spatial position  $\vec{r}$  in the total volume  $V$ , respectively. The equilibrium density profiles follow from a minimization principle  $\delta\Omega/\delta\rho_\nu = 0$  for this functional  $\Omega(T, V, \mu_\nu; [\{\rho_\nu\}])$  at given temperature  $T$ , volume  $V$ , and chemical potentials  $\mu_\nu$  in external potentials  $V_{\text{ext},\nu}(\vec{r})$  [S3, S18]. For technical reasons, the functional typically is split into a free energy contribution

$F_{\text{id}}$  from an ideal gas reference system, a potential contribution  $\sum_{\nu} \int_V \rho_{\nu}(\vec{r})(V_{\text{ext},\nu}(\vec{r}) - \mu_{\nu})d\vec{r}$  from Legendre transforms and the external potentials, and an excess free energy contribution from all pair interactions between the particles [S19]. The latter contribution is typically not known exactly and, for this reason, we used four different approaches, namely the MSAC functional [S4, S20], the  $\delta$ - and  $\theta$ -functional [S21], and the electrostatic mean-field functional [S19]. All these electrostatic contributions were supplemented by a hard-sphere contribution from fundamental measure theory [S22, S23], the so-called White-Bear mark II version [S24].

The MSAC functional and the  $\delta$ - and  $\theta$ -functional are well-performing approaches to describe correlation functions in the RPM in the framework of DFT [S4, S21]. While the former has been used in a recent study on underscreening [S4], here we present results on underscreening for the other two functionals. The mean-field functional is included for completeness but it consistently predicts the Debye length and thus cannot account for any kind of underscreening. For the MSAC functional, the decay length was extracted from the far-field of the density profiles in a system with a planar charged hard wall which yields the same asymptotic as correlations in bulk [S4]. For the other three functionals, we directly calculate the charge-correlation functions using the so-called Percus trick [S25, S26]. In the Percus trick, one particle in the bulk system is fixed by an external field and the one-body distribution in this field yields the corresponding bulk pair-distribution functions.

In fig. S7 the decay lengths of all our extracted decay contributions are depicted as gray symbols. They clearly show anomalous underscreening, as discussed in detail in the main article. Further, experimental results from [S1] are shown (data listed in table S2). In addition to the MSAC DFT data from [S4], we present results that we calculated via the  $\delta$ - and  $\theta$ -functional DFT approaches [S21] and via an electrostatic mean-field functional, as explained above. The mean-field approach always predicts the Debye length as the screening length and, hence, cannot predict underscreening at all. While the position of the Kirkwood transition from monotonic to oscillatory decay [S13, S27] slightly differs between all three DFT approaches (compare discussion on the Kirkwood point in [S4]), the data from all three approaches share an increase of the decay length that follows roughly the same power law corresponding to regular underscreening. None of the three approaches predicts anomalous underscreening, even though the resolution of the correlation functions is much better than that of our MD results.

We stress that the data from the MSAC functional are taken from [S4] and have been calculated by only varying the concentration, while we varied both concentration and Bjerrum length for the three other functional approaches. All these variations lead evidently to the same curve underlining that within the theory the ratio of screening length and Debye length depends exclusively on  $\sigma/\lambda_D$ . Thus, the regular underscreening predicted by

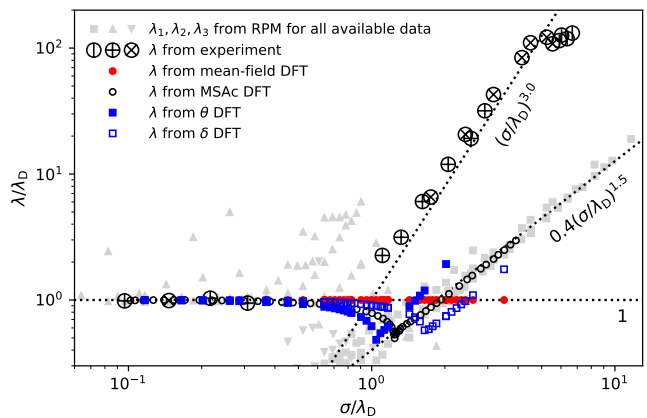


Figure S7. Decay lengths  $\lambda$  in relation to the Debye screening length  $\lambda_D$  as a function of the ratio  $\sigma/\lambda_D$ . Gray symbols present the decay lengths from all decay contributions that we extracted from our MD simulations. Respective data is listed in table S3. Large black circles represent data from experiments on an ionic liquid ( $|$ ), NaCl in water ( $+$ ), and [C4C1Pyr][NTf2] in propylene carbonate ( $\times$ ) [S1]. Dotted lines show power laws as noted. In addition, we re-show decay lengths from DFT calculations using the MSAC functional [S4] that were calculated at fixed Bjerrum length  $\lambda_B = 0.73$  nm and  $\sigma = 0.5$  nm as a function of the concentration. These results are compared against calculations using three other DFT approaches at various concentrations and Bjerrum lengths for  $\sigma = 0.3$  nm.

DFT calculations appears universal in the representation of fig. S7 in contrast to our simulation results for anomalous underscreening.

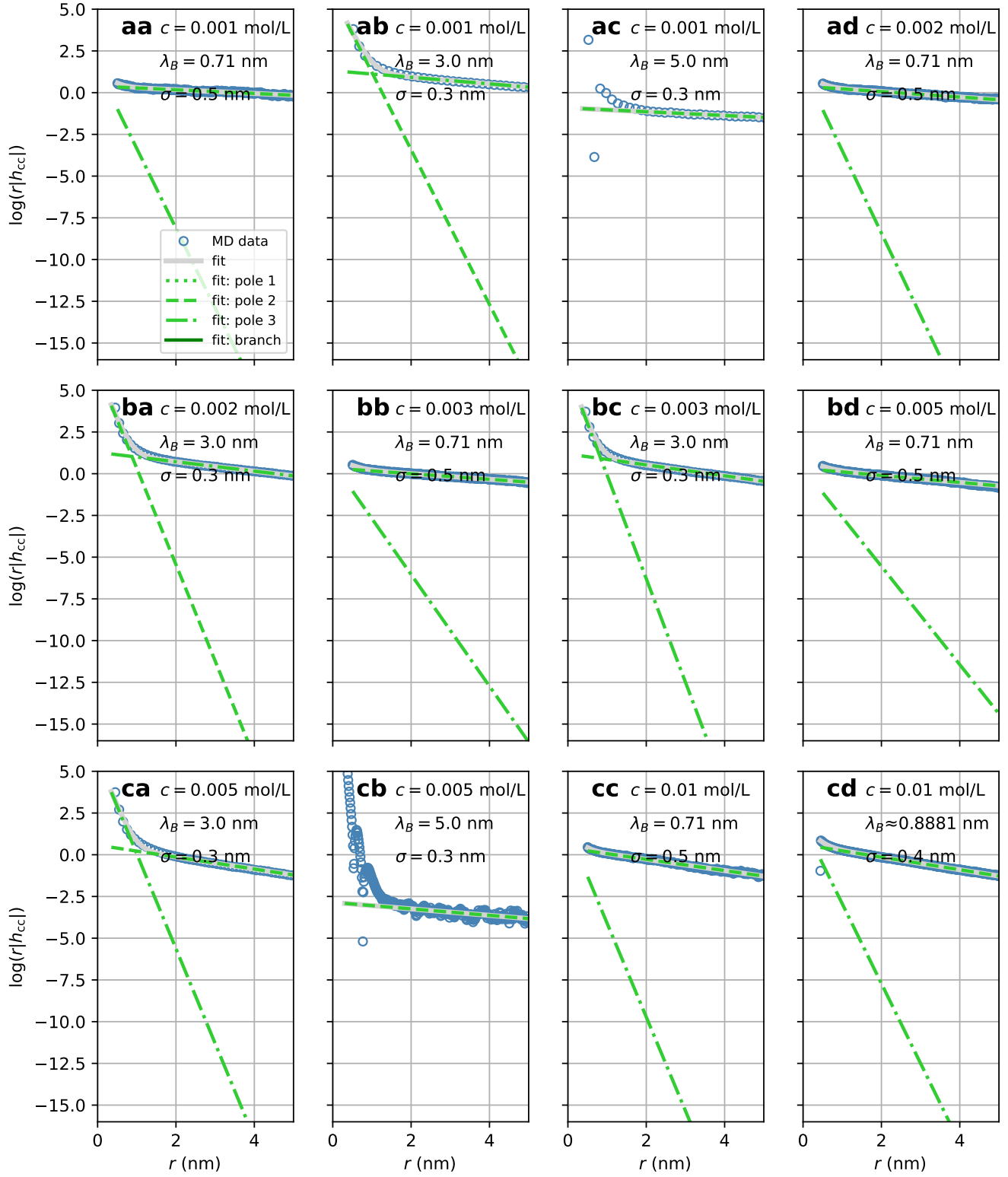


Figure S8. Charge-correlation functions  $h_{cc}(r)$  for parameter sets as indicated and listed in table S3. The pole and branch fits follow eqs. (S8) and (S9) and their sum gives the thick, solid, gray fit function as explained in the text.

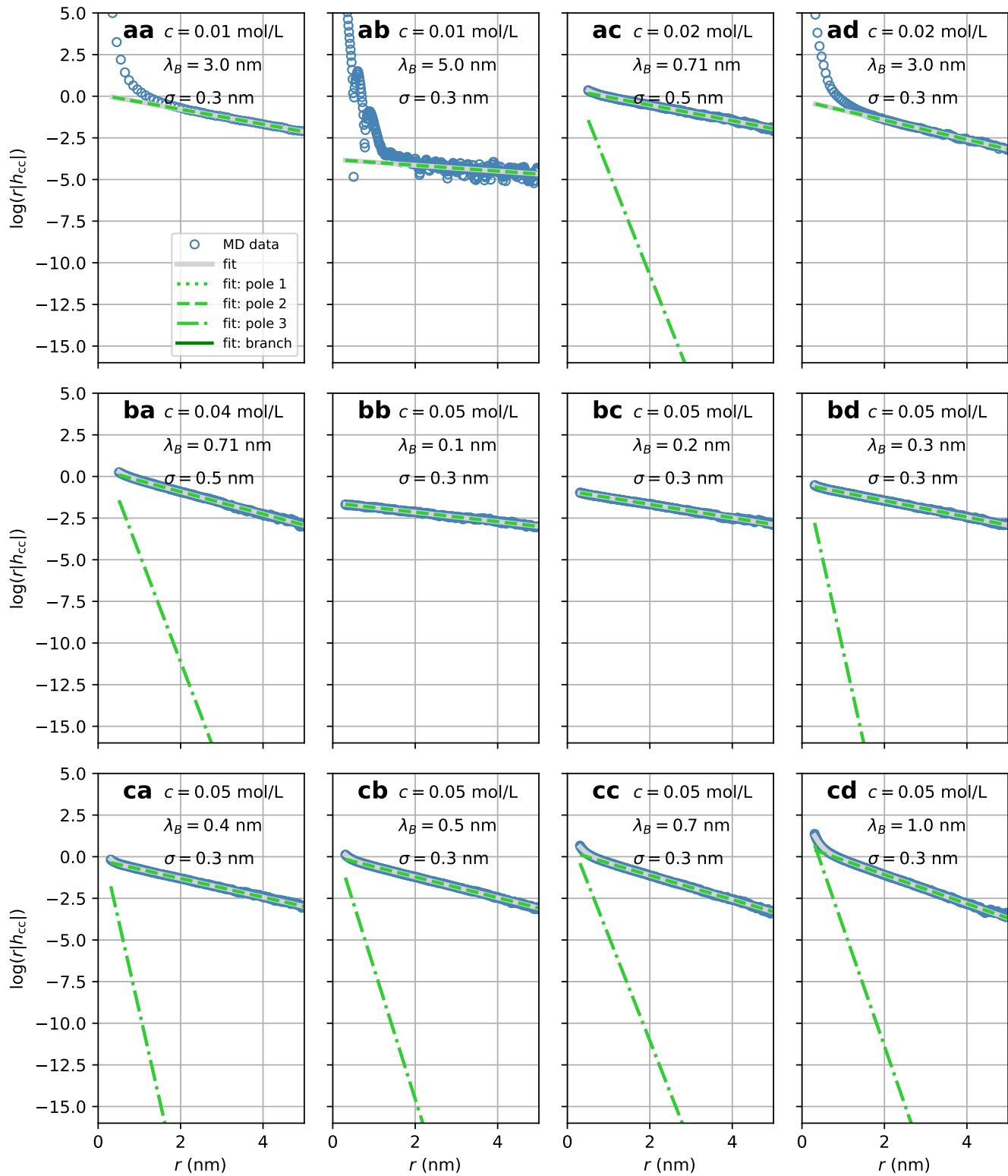


Figure S9. Charge-correlation functions  $h_{cc}(r)$  as explained in fig. S8, but for other parameter sets, as indicated and listed in table S3.



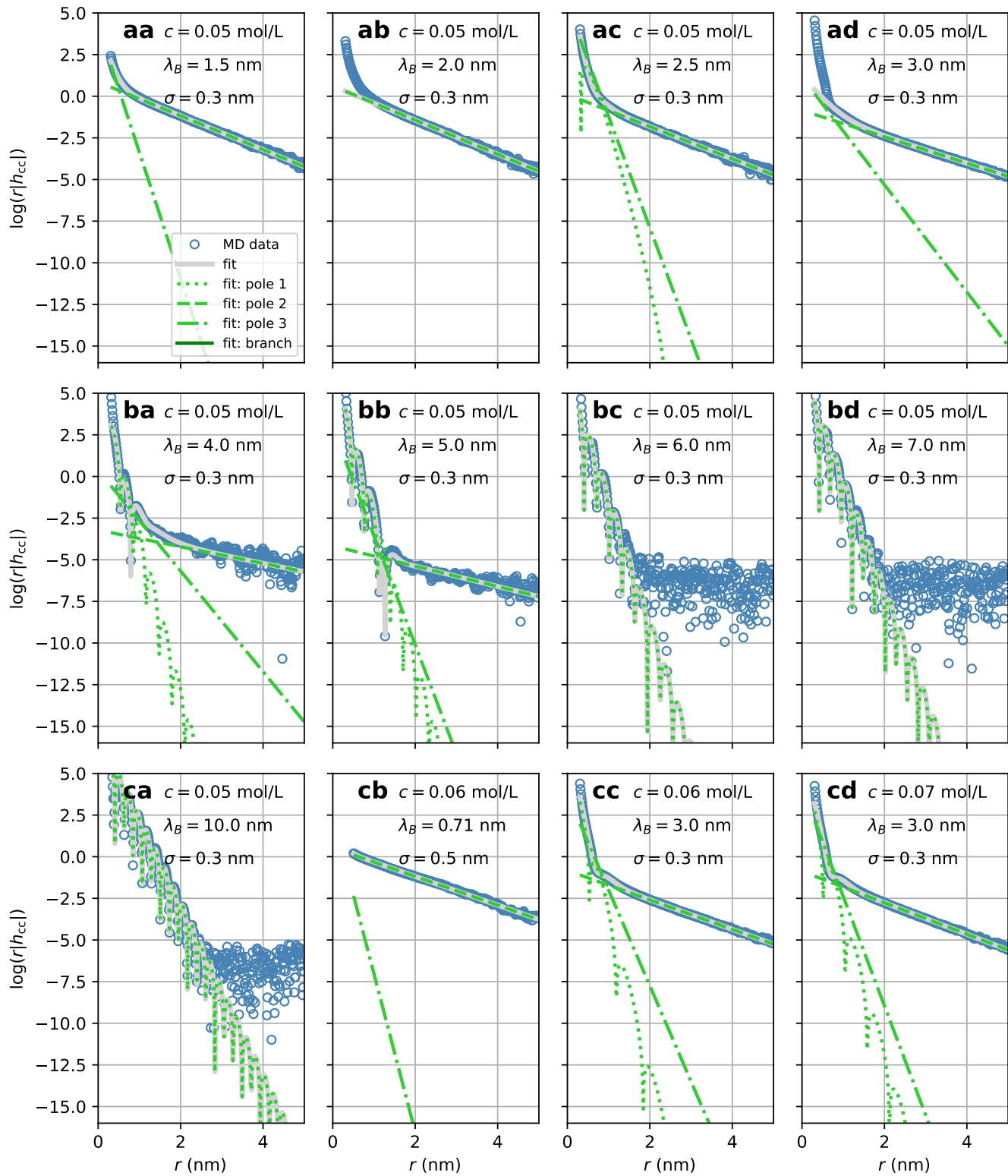


Figure S10. Charge-correlation functions  $h_{cc}(r)$  as explained in fig. S8, but for other parameter sets, as indicated and listed in table S3.

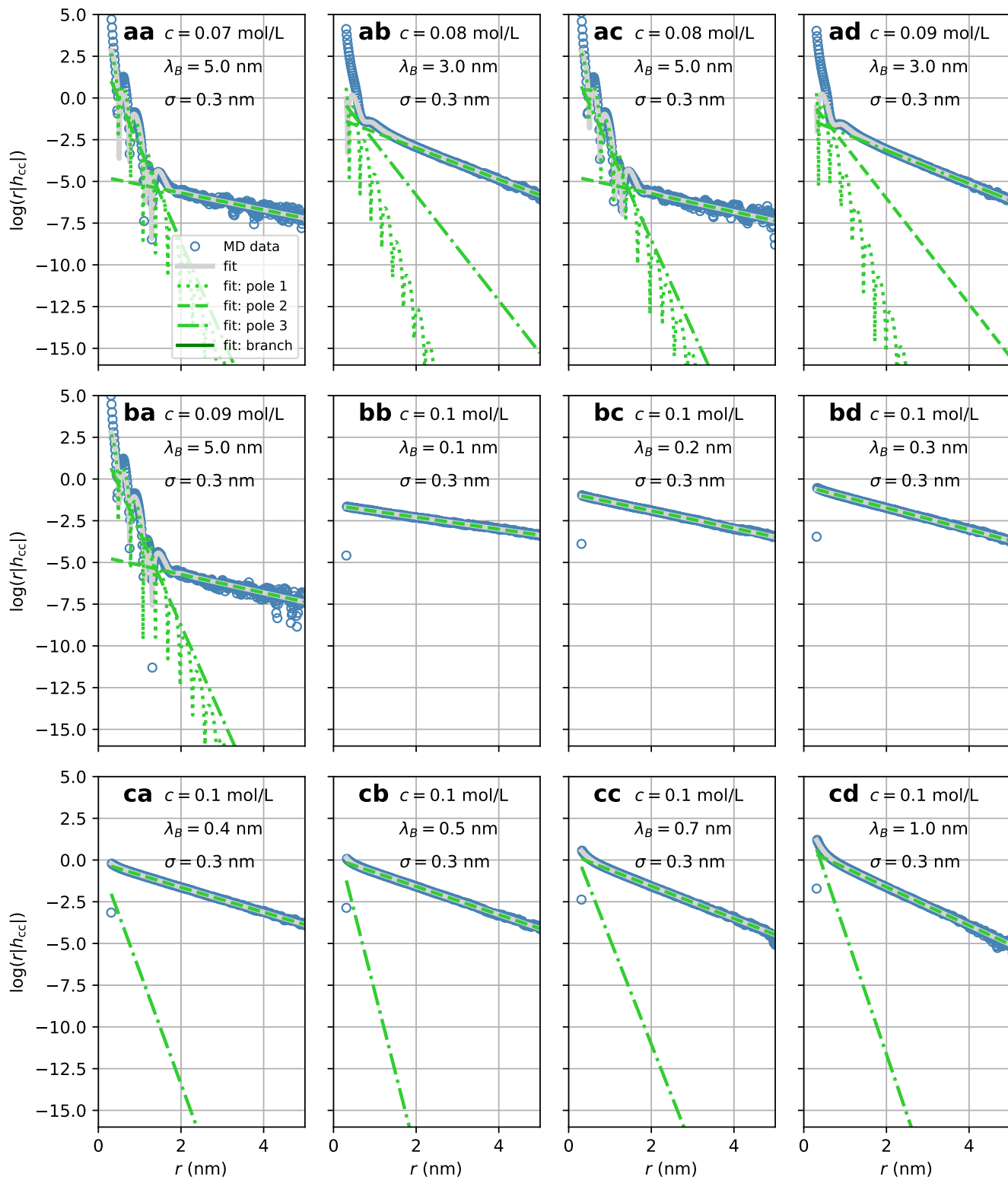


Figure S11. Charge-correlation functions  $h_{cc}(r)$  as explained in fig. S8, but for other parameter sets, as indicated and listed in table S3.

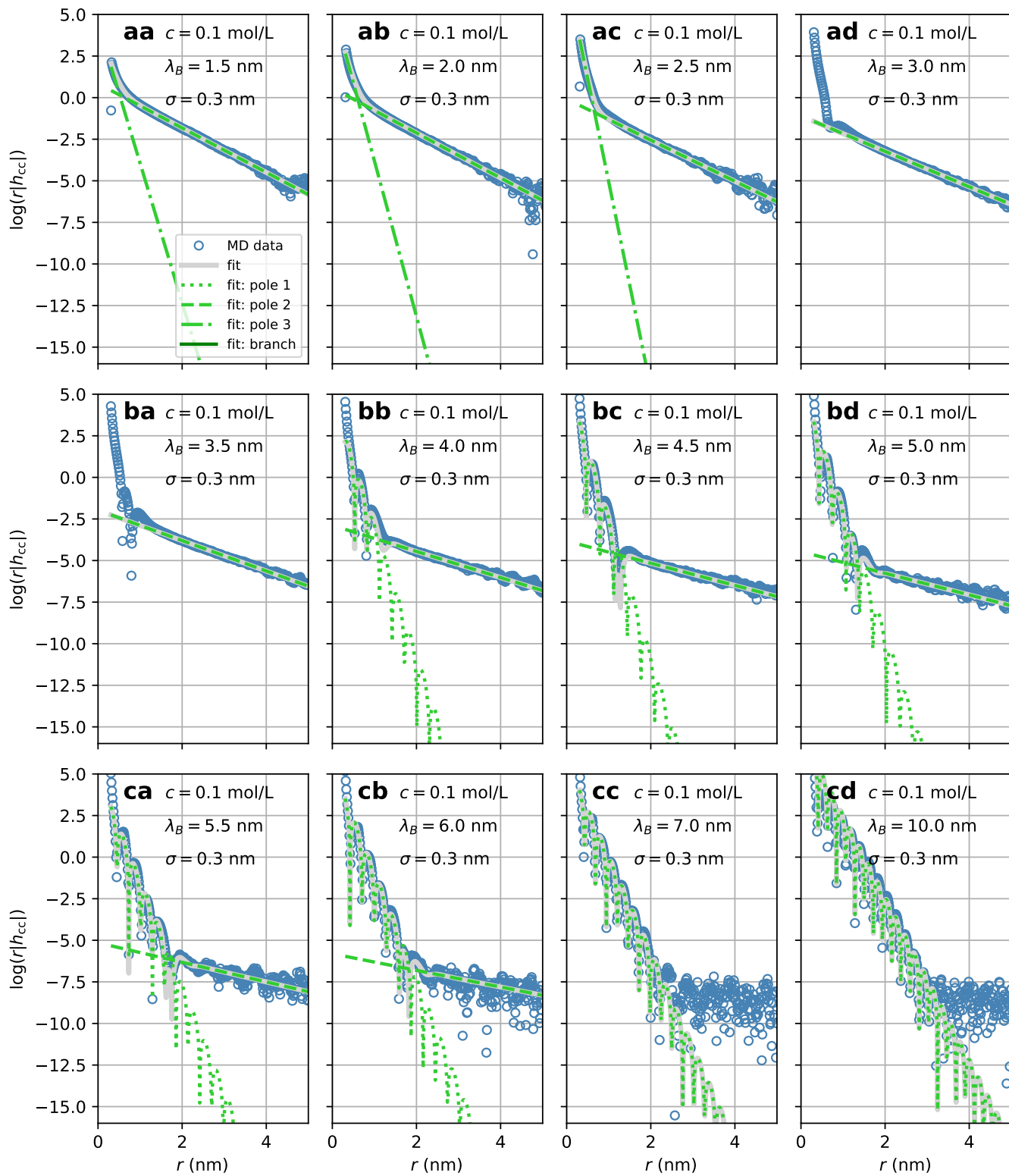


Figure S12. Charge-correlation functions  $h_{cc}(r)$  as explained in fig. S8, but for other parameter sets, as indicated and listed in table S3.

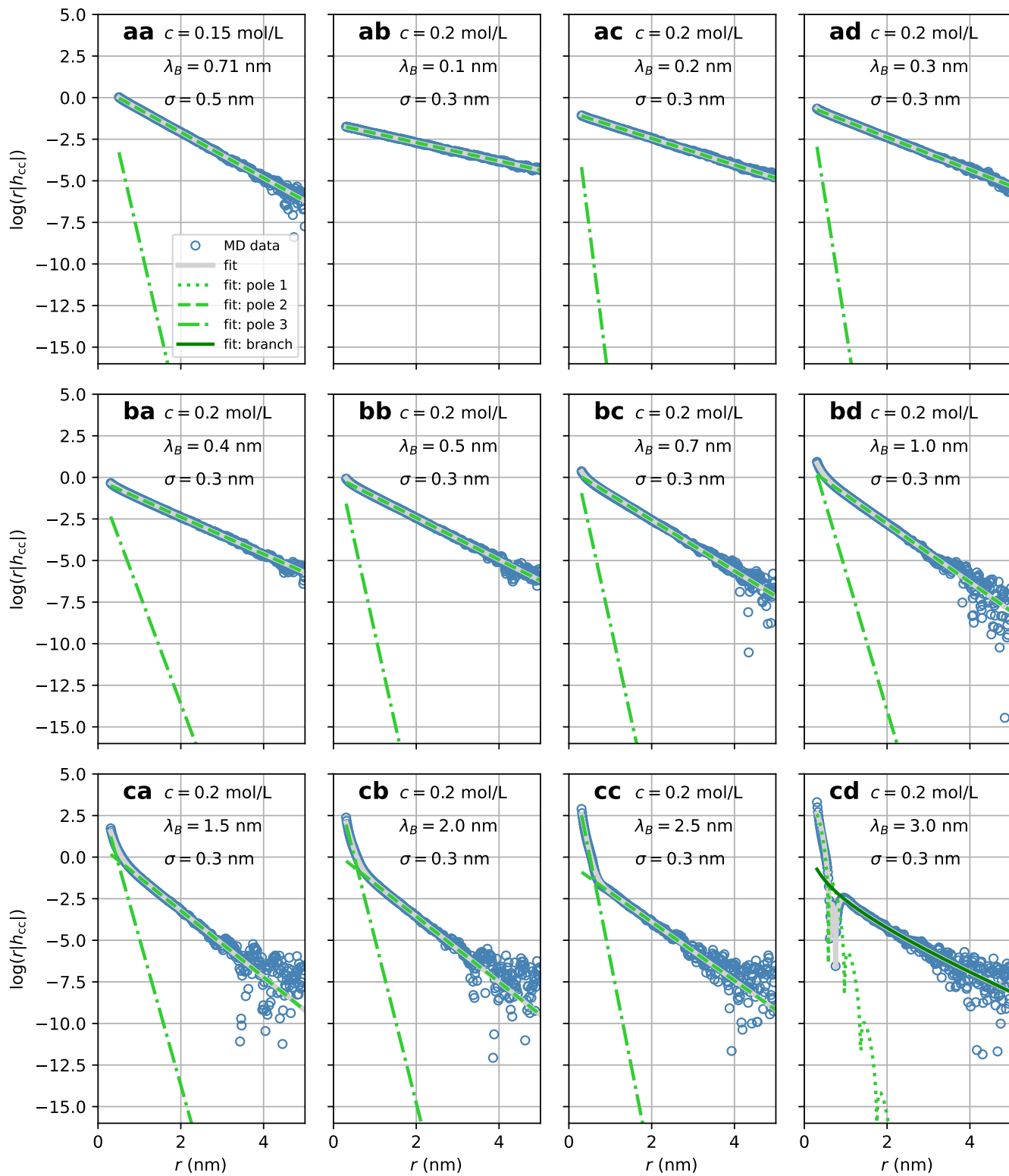


Figure S13. Charge-correlation functions  $h_{cc}(r)$  as explained in fig. S8, but for other parameter sets, as indicated and listed in table S3.

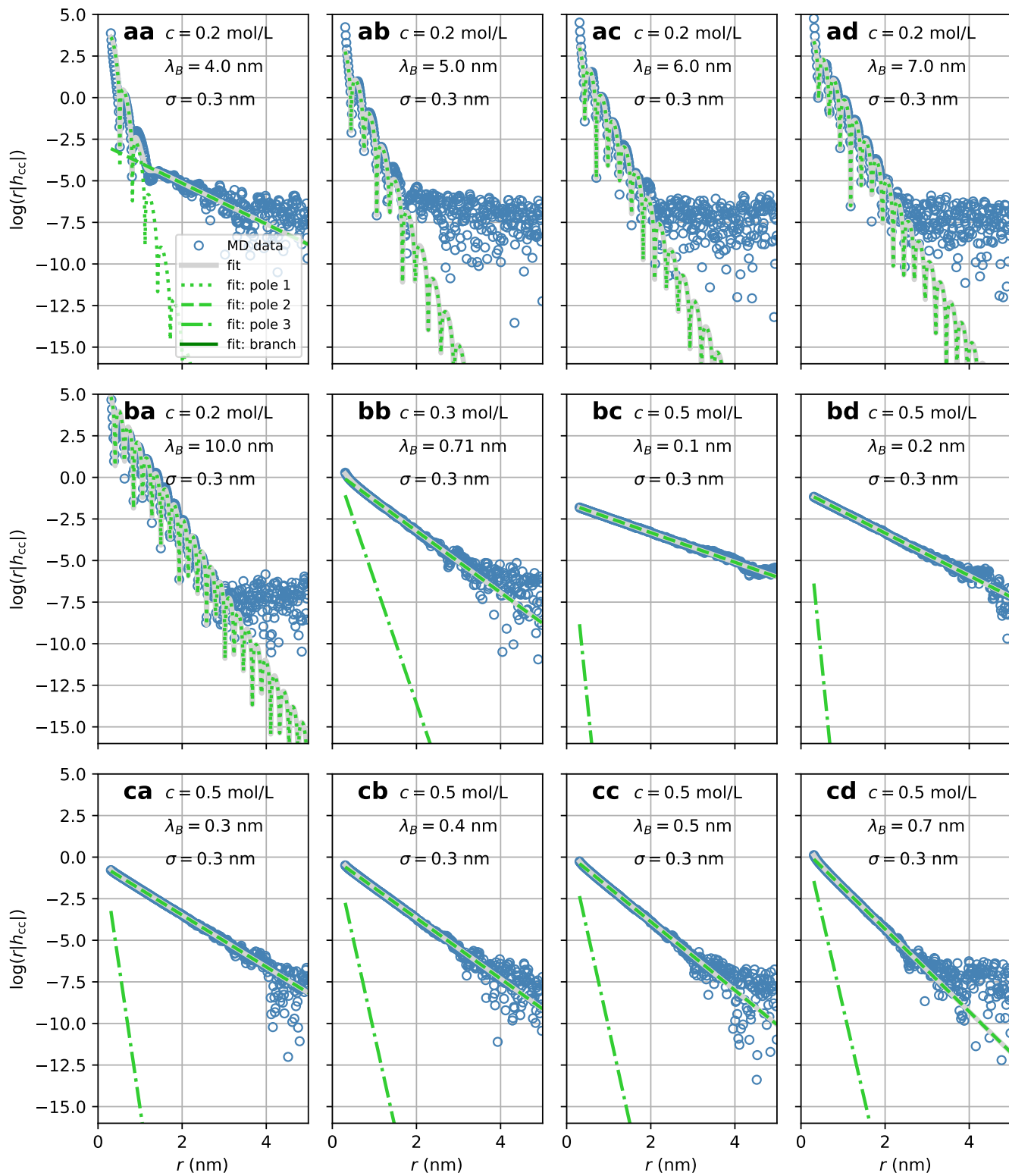


Figure S14. Charge-correlation functions  $h_{cc}(r)$  as explained in fig. S8, but for other parameter sets, as indicated and listed in table S3.

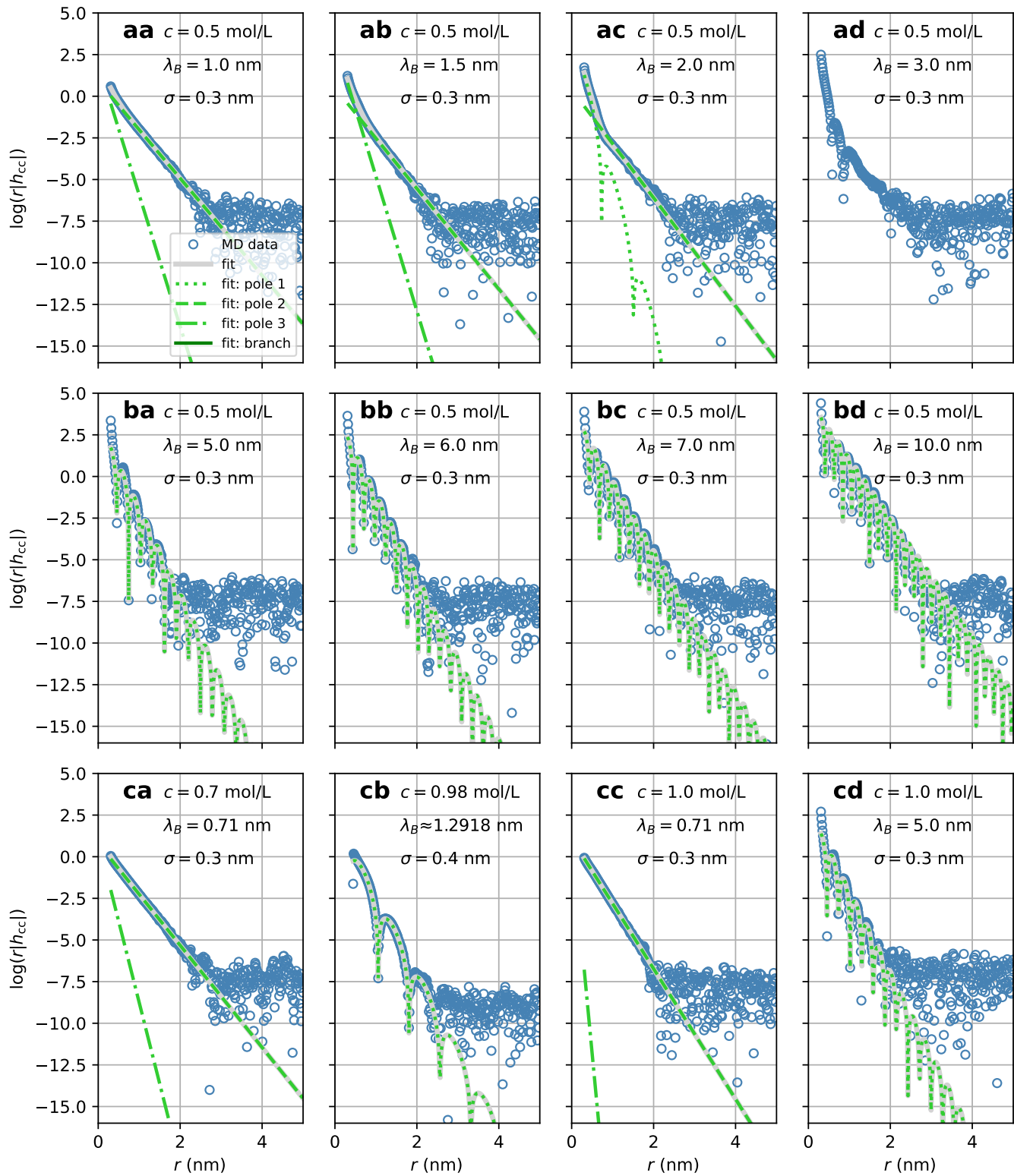


Figure S15. Charge-correlation functions  $h_{cc}(r)$  as explained in fig. S8, but for other parameter sets, as indicated and listed in table S3.



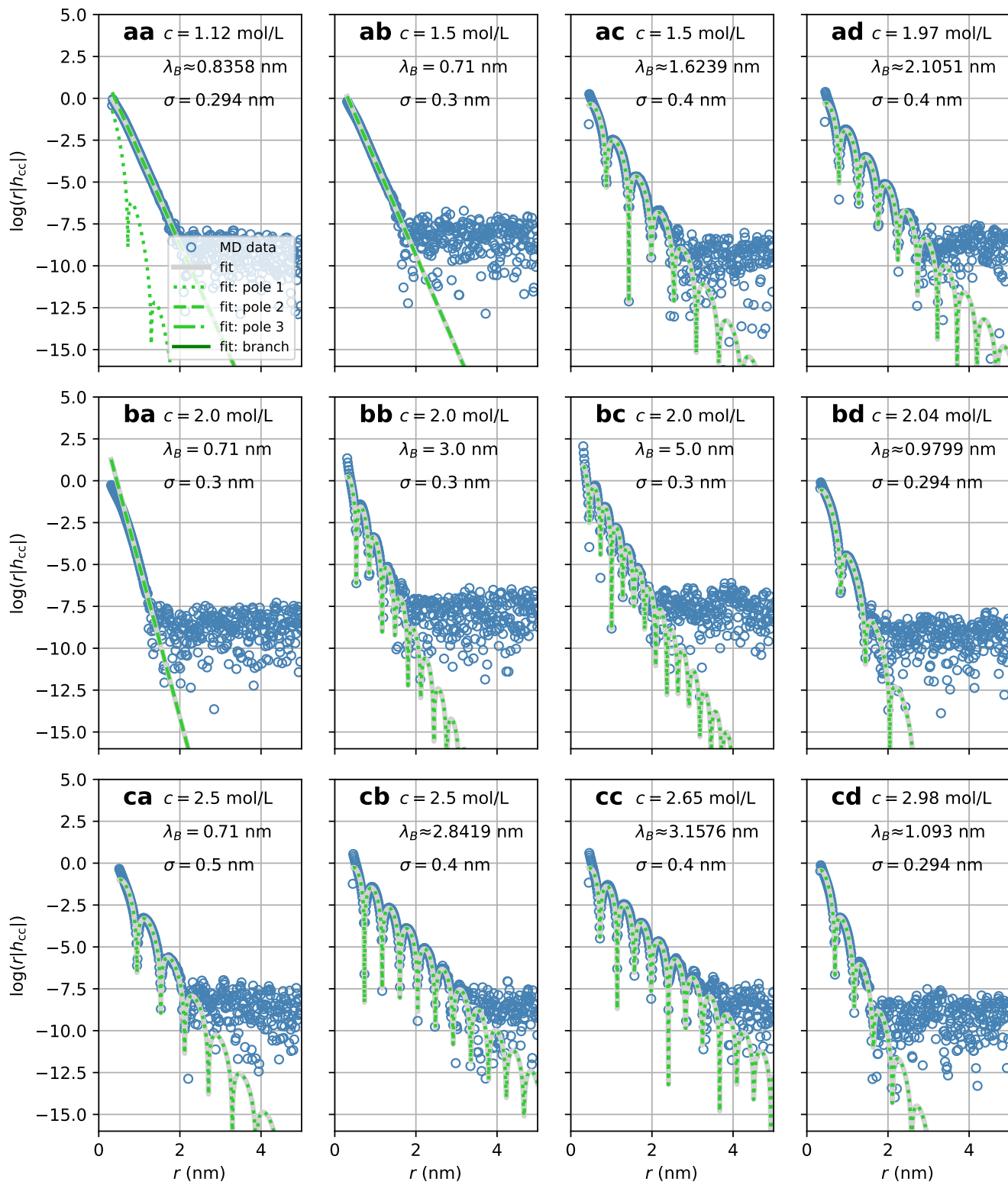


Figure S16. Charge-correlation functions  $h_{cc}(r)$  as explained in fig. S8, but for other parameter sets, as indicated and listed in table S3.

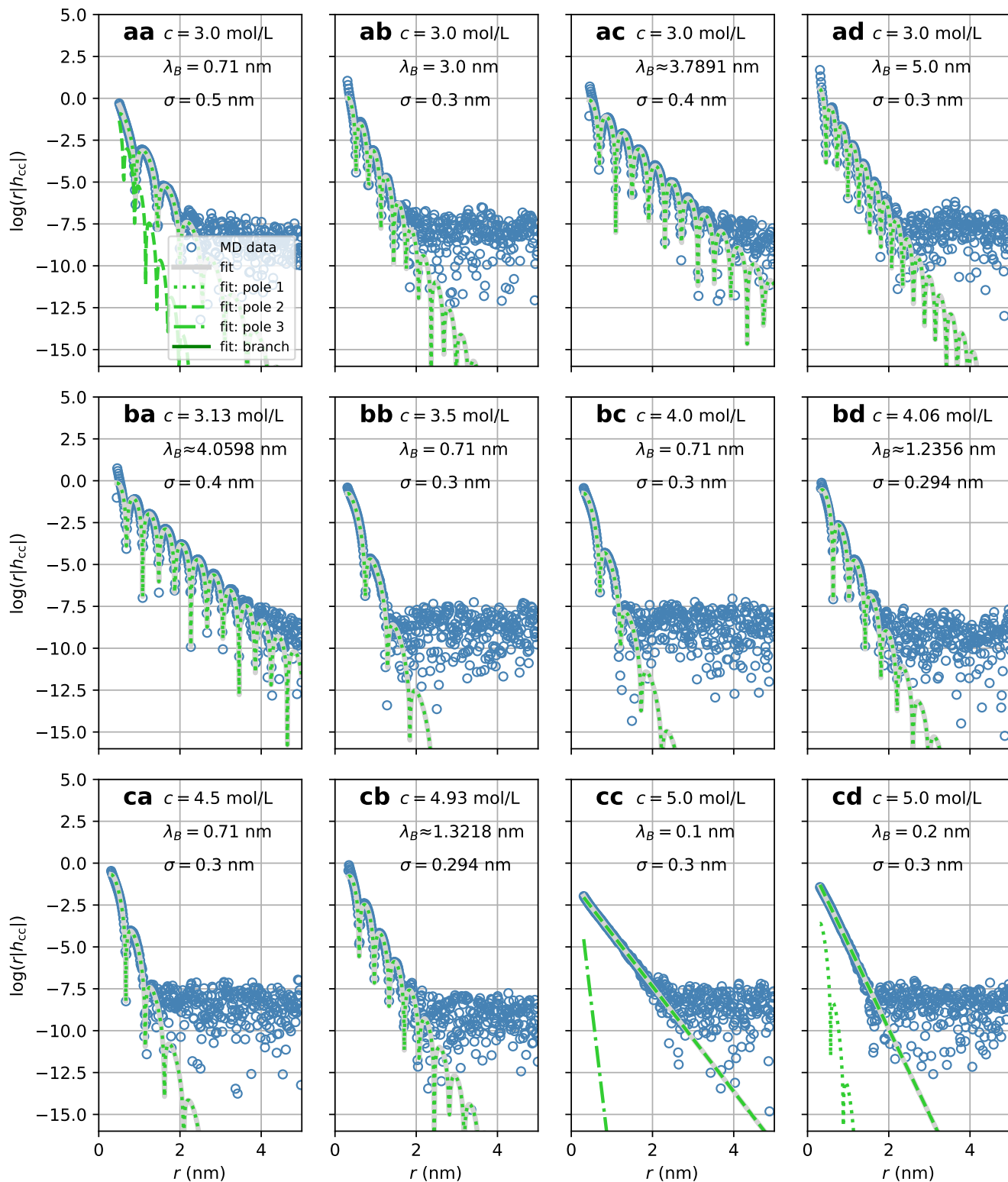


Figure S17. Charge-correlation functions  $h_{cc}(r)$  as explained in fig. S8, but for other parameter sets, as indicated and listed in table S3.

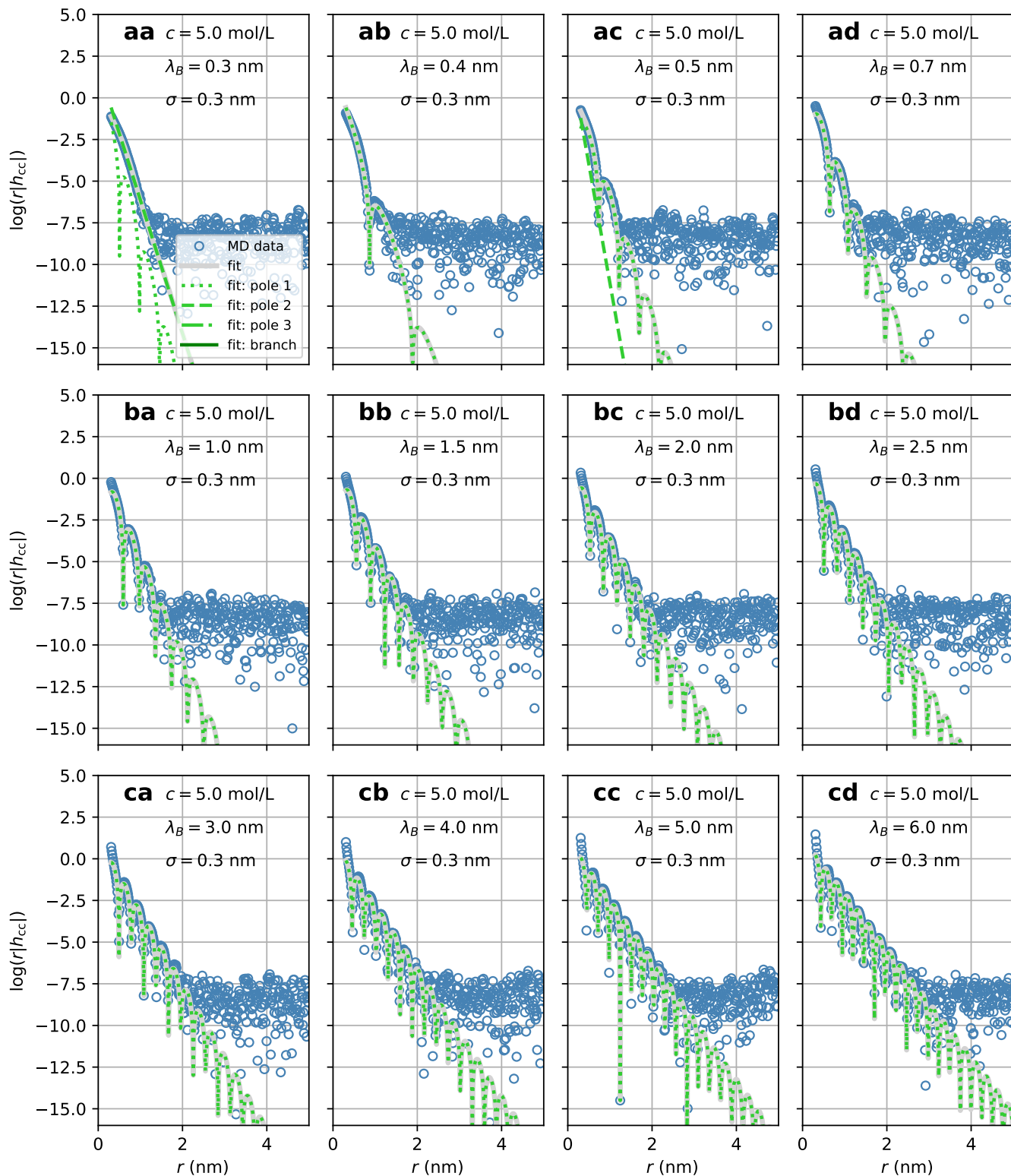


Figure S18. Charge-correlation functions  $h_{cc}(r)$  as explained in fig. S8, but for other parameter sets, as indicated and listed in table S3.

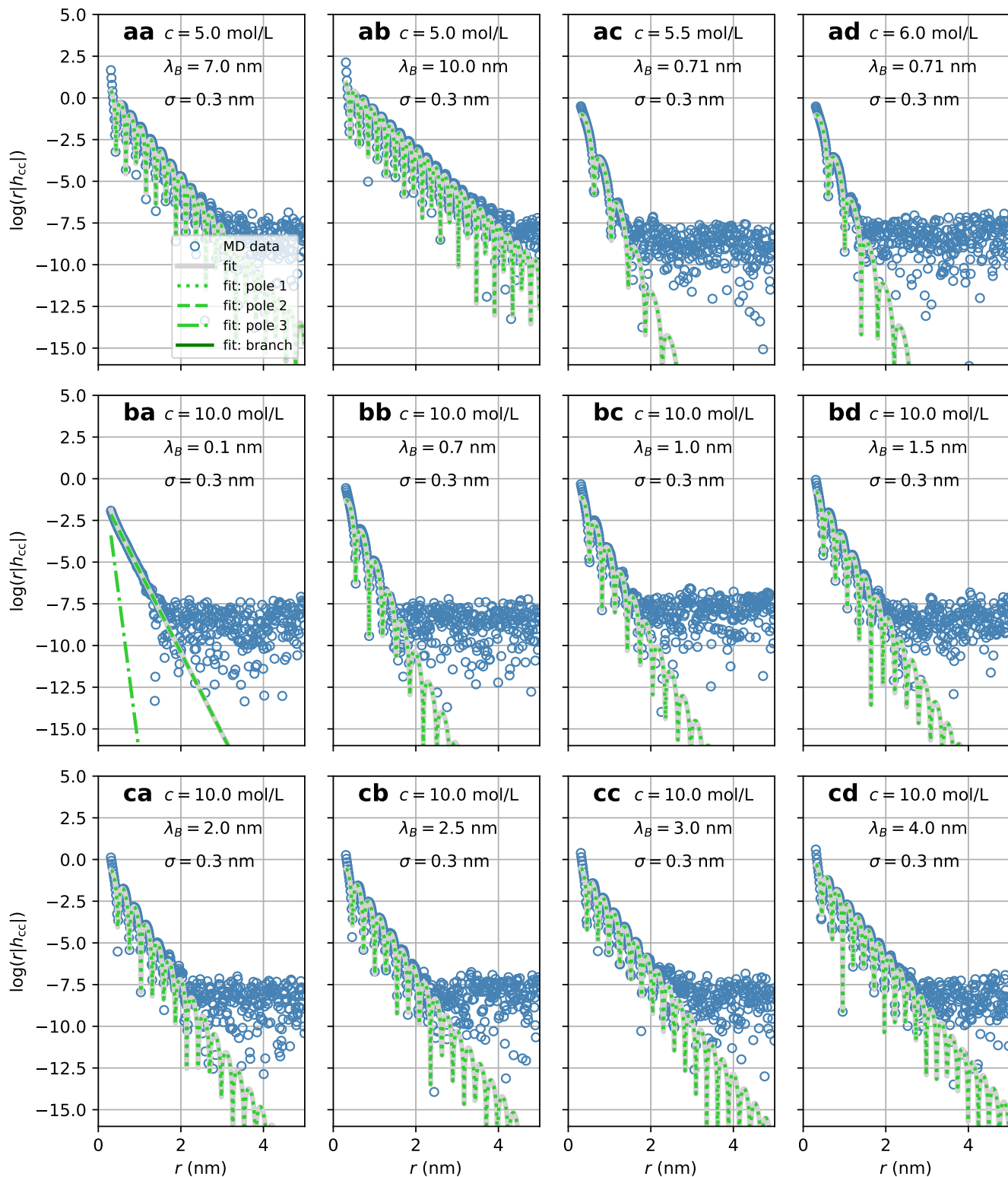


Figure S19. Charge-correlation functions  $h_{cc}(r)$  as explained in fig. S8, but for other parameter sets, as indicated and listed in table S3.

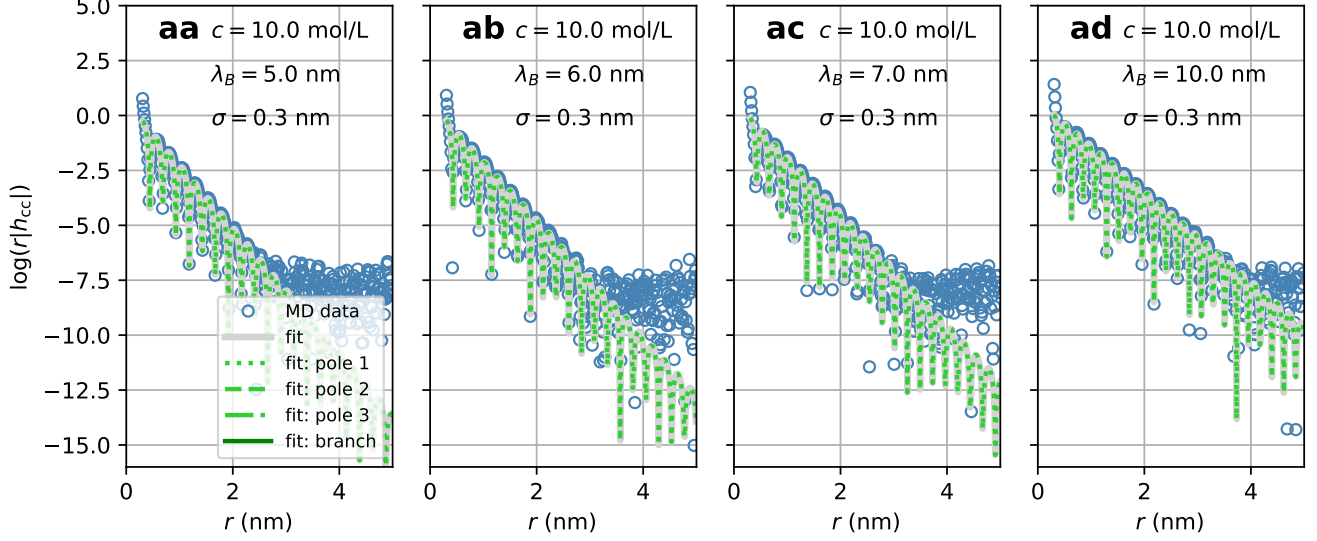


Figure S20. Charge-correlation functions  $h_{cc}(r)$  as explained in fig. S8, but for other parameter sets, as indicated and listed in table S3.

Table S2. Parameter sets as reported for experimental measurements on an ionic liquid, NaCl in water, and [C4C1Pyrr][NTf2] in propylene carbonate from [S1]. We list the reported concentration  $c$ , particle diameter  $\sigma$ , relative permittivity  $\epsilon$ , and the respective measured decay length  $\lambda$ . The experiments are performed at  $T = 294$  K. The Bjerrum length follows via  $\lambda_B = e^2/(4\pi\epsilon_0\epsilon k_B T)$ , with vacuum permittivity  $\epsilon_0$  and elementary charge  $e$ .

	$c$ (mol/L)	$\lambda$ (nm)	$\sigma$ (nm)	$\epsilon$
ionic liquid	3.31	8.4	0.4	12.5
from Table S1 and S4 in [S1]	3.91	7.1	0.38	12.0
	6.54	6.3	0.32	12.9
	5.34	6.6	0.34	15.2
NaCl in water	0.01	3.0	0.294	80.0
from Table S2 and S4(2nd) in [S1]	0.05	1.4	0.294	79.0
	0.10	0.9	0.294	78.0
	1.12	0.6	0.294	68.0
	1.48	0.7	0.294	63.0
	2.04	1.1	0.294	58.0
	2.98	1.7	0.294	52.0
	4.06	2.2	0.294	46.0
	4.93	3.2	0.294	43.0
[C4C1Pyrr][NTf2] in propylene carbonate	0.01	2.7	0.40	64.0
from Table S3 and S5 in [S1]	0.98	1.5	0.40	44.0
	1.50	3.4	0.40	35.0
	1.97	5.4	0.40	27.0
	2.50	8.1	0.40	20.0
	2.65	9.8	0.40	18.0
	3.00	9.3	0.40	15.0
	3.13	7.8	0.40	14.0

Table S3: Relevant parameters and extracted data for all MD simulations we performed. Simulation parameters are the concentration  $c$  of ions, the Bjerrum length  $\lambda_B$ , the ion diameter  $\sigma$ , the length  $L_z$  of the simulation box, and the number  $N_g$  of samples used for sampling a pair-distribution function. For convenience we also list the ratio  $\sigma/\lambda_D$  of ion diameter and Debye length. For each simulation we further list the parameters for each extracted pole or branch point and its corresponding decay length  $\lambda$ . The first column refers to the figure and panel where the respective pair charge-correlation function and the fit functions from poles and branch points are shown.

Figure	$c$ (mol/L)	$\lambda_B$ (nm)	$\sigma$ (nm)	$\sigma/\lambda_D$	$L$ (nm)	$N_g$	pole: $rh_{cc}(r) = a \cdot \exp(-b \cdot r) \cos(c \cdot r + d)$ branch: $rh_{cc}(r) = a \cdot \exp(-b \cdot r) \cos(c \cdot r + d)/r$	$\lambda$	$\lambda/\lambda_D$
							$\begin{matrix} a & b & c & d \end{matrix}$		
8(aa)	0.001	0.71	0.5	0.05(1)	120	74148	pole 2: 1.478(8) 0.109(9) 0.0 0.0 pole 3: 4.199(6) 4.782(2) 0.0 0.0	9.092(7) 0.94(2) 0.209(1) 0.02(1)	
8(ab)	0.001	3.0	0.3	0.06(3)	200	1268532	pole 2: 347.069(0) 4.635(6) 0.0 0.0 pole 3: 3.721(7) 0.196(8) 0.0 0.0	0.215(7) 0.04(5) 5.081(0) 1.08(2)	
8(ac)	0.001	5.0	0.3	0.08(2)	200	1230957	pole 2: 0.4 0.113 0.0 0.0	8.849(5) 2.43(4)	
8(ad)	0.002	0.71	0.5	0.07(3)	120	64128	pole 2: 1.469(9) 0.162(1) 0.0 0.0 pole 3: 4.286(8) 4.933(6) 0.0 0.0	6.168(6) 0.90(4) 0.202(6) 0.02(9)	
8(ba)	0.002	3.0	0.3	0.09(0)	120	824145	pole 2: 444.217(1) 5.771(9) 0.0 0.0 pole 3: 3.598(3) 0.282(1) 0.0 0.0	0.173(2) 0.05(2) 3.543(8) 1.06(7)	
8(bb)	0.003	0.71	0.5	0.08(9)	120	54108	pole 2: 1.396(6) 0.167(5) 0.0 0.0 pole 3: 1.919(0) 3.345(8) 0.0 0.0	5.968(1) 1.07(1) 0.298(8) 0.05(3)	
8(bc)	0.003	3.0	0.3	0.11(0)	120	706331	pole 2: 3.264(4) 0.327(6) 0.0 0.0 pole 3: 453.512(1) 6.202(1) 0.0 0.0	3.052(2) 1.12(6) 0.161(2) 0.05(9)	
8(bd)	0.005	0.71	0.5	0.11(5)	120	19038	pole 2: 1.365(7) 0.208(0) 0.0 0.0 pole 3: 1.405(4) 2.944(7) 0.0 0.0	4.806(8) 1.11(4) 0.339(5) 0.07(8)	
8(ca)	0.005	3.0	0.3	0.14(2)	120	886269	pole 2: 1.778(0) 0.357(9) 0.0 0.0 pole 3: 310.124(8) 5.680(8) 0.0 0.0	2.793(8) 1.33(0) 0.176(0) 0.08(3)	
8(cb)	0.005	5.0	0.3	0.18(4)	120	1098693	pole 2: 0.057(6) 0.194(7) 0.0 0.0	5.133(4) 3.15(7)	
8(cc)	0.01	0.71	0.5	0.16(3)	30	19038	pole 2: 1.493(3) 0.337(1) 0.0 0.0 pole 3: 4.588(2) 5.621(4) 0.0 0.0	2.966(3) 0.97(2) 0.177(8) 0.05(8)	
8(cd)	0.01	$\approx 0.8881$	0.4	0.14(6)	60	184368	pole 2: 1.841(2) 0.376(9) 0.0 0.0 pole 3: 6.381(9) 4.784(4) 0.0 0.0	2.652(9) 0.97(2) 0.209(0) 0.07(6)	
9(aa)	0.01	3.0	0.3	0.20(2)	120	391281	pole 2: 1.111(7) 0.446(5) 0.0 0.0	2.239(6) 1.50(8)	
9(ab)	0.01	5.0	0.3	0.26(0)	120	693384	pole 2: 0.022(5) 0.175 0.0 0.0	5.714(2) 4.97(0)	
9(ac)	0.02	0.71	0.5	0.23(1)	60	19038	pole 2: 1.518(6) 0.472(5) 0.0 0.0 pole 3: 5.565(0) 6.223(8) 0.0 0.0	2.116(2) 0.98(0) 0.160(6) 0.07(4)	
9(ad)	0.02	3.0	0.3	0.28(5)	60	480960	pole 2: 0.761(8) 0.582(1) 0.0 0.0	1.717(7) 1.63(6)	
9(ba)	0.04	0.71	0.5	0.32(7)	60	16533	pole 2: 1.528(2) 0.669(7) 0.0 0.0 pole 3: 6.420(8) 6.495(1) 0.0 0.0	1.493(0) 0.97(8) 0.153(9) 0.10(0)	
9(bb)	0.05	0.1	0.3	0.08(2)	60	32064	pole 2: 0.205(6) 0.282(4) 0.0 0.0	3.540(2) 0.97(3)	
9(bc)	0.05	0.2	0.3	0.11(6)	60	32064	pole 2: 0.419(7) 0.403(1) 0.0 0.0	2.480(2) 0.96(4)	
9(bd)	0.05	0.3	0.3	0.14(2)	60	32064	pole 2: 0.624(9) 0.491(3) 0.0 0.0 pole 3: 1.838(3) 11.088(8) 0.0 0.0	2.035(0) 0.96(9) 0.090(1) 0.04(2)	
9(ca)	0.05	0.4	0.3	0.16(5)	60	32064	pole 2: 0.830(1) 0.560(5) 0.0 0.0 pole 3: 4.696(0) 10.844(9) 0.0 0.0	1.784(1) 0.98(1) 0.092(2) 0.05(0)	
9(cb)	0.05	0.5	0.3	0.18(4)	60	32064	pole 2: 1.031(1) 0.622(5) 0.0 0.0 pole 3: 3.169(0) 7.855(0) 0.0 0.0	1.606(2) 0.98(7) 0.127(3) 0.07(8)	
9(cc)	0.05	0.7	0.3	0.21(8)	60	31563	pole 2: 1.409(2) 0.730(0) 0.0 0.0 pole 3: 4.641(5) 6.288(9) 0.0 0.0	1.369(7) 0.99(6) 0.159(0) 0.11(5)	
9(cd)	0.05	1.0	0.3	0.26(0)	60	32064	pole 2: 1.947(4) 0.872(1) 0.0 0.0 pole 3: 17.966(4) 7.130(2) 0.0 0.0	1.146(5) 0.99(7) 0.140(2) 0.12(1)	
10(aa)	0.05	1.5	0.3	0.31(9)	60	32064	pole 2: 2.371(1) 1.018(3) 0.0 0.0 pole 3: 67.251(9) 7.575(1) 0.0 0.0	0.981(9) 1.04(6) 0.132(0) 0.14(0)	
10(ab)	0.05	2.0	0.3	0.36(9)	60	32064	pole 2: 1.846(9) 1.024(1) 0.0 0.0	0.976(3) 1.20(0)	
10(ac)	0.05	2.5	0.3	0.41(2)	60	32064	pole 1: 2010.106(4) 9.264(4) 1.504(9) 1.073(4) pole 2: 1.115(8) 0.967(8) 0.0 0.0 pole 3: 241.112(3) 6.689(4) 0.0 0.0	0.107(9) 0.14(8) 1.033(2) 1.42(0) 0.149(4) 0.20(5)	
10(ad)	0.05	3.0	0.3	0.45(1)	60	1088172	pole 2: 0.427(4) 0.792(2) 0.0 0.0 pole 3: 3.105(2) 3.223(3) 0.0 0.0	1.262(2) 1.90(1) 0.310(2) 0.46(7)	
10(ba)	0.05	4.0	0.3	0.52(1)	60	32064	pole 1: 499.825(9) 9.397(1) 10.046(1) 2.449(1) pole 2: 0.04 0.5 0.0 0.0 pole 3: 1.448(5) 3.021(9) 0.0 0.0	0.106(4) 0.18(5) 2.0 3.47(9) 0.330(9) 0.57(5)	
10(bb)	0.05	5.0	0.3	0.58(3)	60	1181358	pole 1: 820.302(8) 8.740(1) 10.065(5) -3.067(0) pole 2: 0.015(4) 0.608(0) 0.0 0.0 pole 3: 19.345(9) 6.536(1) 0.0 0.0	0.114(4) 0.22(2) 1.644(7) 3.19(8) 0.152(9) 0.29(7)	
10(bc)	0.05	6.0	0.3	0.63(9)	60	32064	pole 1: 621.937(7) 7.464(6) 10.213(2) 0.567(6)	0.133(9) 0.28(5)	
10(bd)	0.05	7.0	0.3	0.69(0)	60	32064	pole 1: 683.114(3) 6.538(0) 11.775(3) 2.925(9)	0.152(9) 0.35(1)	
10(ca)	0.05	10.0	0.3	0.82(5)	60	32064	pole 1: 1978.496(8) 5.131(7) 14.247(8) -1.066(8)	0.194(8) 0.53(5)	
10(cb)	0.06	0.71	0.5	0.40(1)	60	14028	pole 2: 1.716(4) 0.862(1) 0.0 0.0	1.159(8) 0.93(1)	

Table continues on the next page



Table S3: Continuation from previous page

Figure	$c$ (mol/L)	$\lambda_B$ (nm)	$\sigma$ (nm)	$\sigma/\lambda_D$	$L$ (nm)	$N_g$	$a$ (1)	$b$ (1/nm)	$c$ (1/nm)	$d$ (1)	$\lambda$ (nm)	$\lambda/\lambda_D$
10(cc)	0.06	3.0	0.3	0.49(5)	60	975948	pole 3: 11.645(3)	9.488(3)	0.0	0.0	0.105(3)	0.08(4)
							pole 1: 539.340(5)	9.325(4)	4.812(7)	-1.005(2)	0.107(2)	0.17(6)
							pole 2: 0.438(1)	0.884(0)	0.0	0.0	1.131(2)	1.86(6)
10(cd)	0.07	3.0	0.3	0.53(4)	60	924345	pole 3: 42.502(2)	5.748(1)	0.0	0.0	0.173(9)	0.28(7)
							pole 1: 217.213(8)	8.434(1)	5.860(7)	-1.440(2)	0.118(5)	0.21(1)
							pole 2: 0.416(5)	0.944(8)	0.0	0.0	1.058(3)	1.88(6)
							pole 3: 64.902(8)	6.561(7)	0.0	0.0	0.152(3)	0.27(1)
11(aa)	0.07	5.0	0.3	0.69(0)	60	1092681	pole 1: 120.001(6)	6.770(4)	10.509(5)	2.771(2)	0.147(6)	0.33(9)
							pole 2: 0.009(3)	0.506(7)	0.0	0.0	1.973(3)	4.54(0)
							pole 3: 15.925(5)	5.712(1)	0.0	0.0	0.175(0)	0.40(2)
11(ab)	0.08	3.0	0.3	0.57(1)	60	750999	pole 1: 25.132(6)	7.721(9)	12.012(9)	0.138(7)	0.129(5)	0.24(6)
							pole 2: 0.328(0)	0.941(6)	0.0	0.0	1.061(9)	2.02(3)
							pole 3: 1.657(9)	3.160(0)	0.0	0.0	0.316(4)	0.60(3)
11(ac)	0.08	5.0	0.3	0.73(8)	60	967544	pole 1: 120.002(1)	6.704(3)	10.602(0)	2.699(7)	0.149(1)	0.36(6)
							pole 2: 0.009(5)	0.543(0)	0.0	0.0	1.841(5)	4.53(0)
							pole 3: 10.665(3)	5.436(3)	0.0	0.0	0.183(9)	0.45(2)
11(ad)	0.09	3.0	0.3	0.60(6)	60	826650	pole 1: 25.467(1)	7.650(6)	11.537(8)	0.598(9)	0.130(7)	0.26(4)
							pole 2: 1.383(2)	3.169(0)	0.0	0.0	0.315(5)	0.63(7)
							pole 3: 0.314(7)	0.993(5)	0.0	0.0	1.006(4)	2.03(4)
11(ba)	0.09	5.0	0.3	0.78(2)	60	843181	pole 1: 120.0	6.799(9)	10.5	2.783(1)	0.147(0)	0.38(3)
							pole 2: 0.009(9)	0.550(5)	0.0	0.0	1.816(2)	4.73(9)
							pole 3: 10.659(2)	5.567(4)	0.0	0.0	0.179(6)	0.46(8)
11(bb)	0.1	0.1	0.3	0.11(6)	60	26049	pole 2: 0.207(2)	0.357(5)	0.0	0.0	2.796(8)	1.08(7)
11(bc)	0.1	0.2	0.3	0.16(5)	60	26052	pole 2: 0.425(2)	0.523(4)	0.0	0.0	1.910(2)	1.05(0)
11(bd)	0.1	0.3	0.3	0.20(2)	60	26052	pole 2: 0.653(5)	0.652(7)	0.0	0.0	1.532(0)	1.03(2)
11(ca)	0.1	0.4	0.3	0.23(3)	60	26052	pole 2: 0.867(5)	0.746(3)	0.0	0.0	1.339(9)	1.04(2)
							pole 3: 1.079(3)	6.748(7)	0.0	0.0	0.148(1)	0.11(5)
11(cb)	0.1	0.5	0.3	0.26(0)	60	26052	pole 2: 1.104(5)	0.841(9)	0.0	0.0	1.187(7)	1.03(3)
							pole 3: 5.940(7)	9.686(8)	0.0	0.0	0.103(2)	0.08(9)
11(cc)	0.1	0.7	0.3	0.30(8)	60	26052	pole 2: 1.456(5)	0.969(4)	0.0	0.0	1.031(5)	1.06(1)
							pole 3: 4.724(9)	6.292(2)	0.0	0.0	0.158(9)	0.16(3)
11(cd)	0.1	1.0	0.3	0.36(9)	60	26052	pole 2: 1.981(7)	1.150(2)	0.0	0.0	0.869(4)	1.06(9)
							pole 3: 18.312(4)	7.270(5)	0.0	0.0	0.137(5)	0.16(9)
12(aa)	0.1	1.5	0.3	0.45(1)	60	26052	pole 2: 2.320(4)	1.334(2)	0.0	0.0	0.749(4)	1.12(9)
							pole 3: 85.828(5)	8.392(4)	0.0	0.0	0.119(1)	0.17(9)
12(ab)	0.1	2.0	0.3	0.52(1)	60	26052	pole 2: 1.790(5)	1.353(6)	0.0	0.0	0.738(7)	1.28(5)
							pole 3: 259.287(1)	9.358(5)	0.0	0.0	0.106(8)	0.18(5)
12(ac)	0.1	2.5	0.3	0.58(3)	60	26052	pole 2: 0.917(7)	1.235(7)	0.0	0.0	0.809(2)	1.57(3)
							pole 3: 1528.0	12.4	0.0	0.0	0.080(6)	0.15(6)
12(ad)	0.1	3.0	0.3	0.63(9)	60	578649	pole 2: 0.332(7)	1.065(4)	0.0	0.0	0.938(5)	1.99(9)
12(ba)	0.1	3.5	0.3	0.69(0)	60	969432	pole 2: 0.138(5)	0.913(1)	0.0	0.0	1.095(0)	2.51(9)
12(bb)	0.1	4.0	0.3	0.73(8)	60	995982	pole 1: 131.943(7)	7.734(2)	10.617(2)	2.215(8)	0.129(2)	0.31(8)
							pole 2: 0.055(8)	0.784(8)	0.0	0.0	1.274(2)	3.13(4)
12(bc)	0.1	4.5	0.3	0.78(2)	60	1510004	pole 1: 350.0	8.259(7)	9.682(9)	-2.953(5)	0.121(0)	0.31(5)
							pole 2: 0.021(7)	0.667(9)	0.0	0.0	1.497(2)	3.90(6)
12(bd)	0.1	5.0	0.3	0.82(5)	60	1546754	pole 1: 303.511(5)	7.509(2)	9.8	-2.641(5)	0.133(1)	0.36(6)
							pole 2: 0.011(5)	0.65	0.0	0.0	1.538(4)	4.23(1)
12(ca)	0.1	5.5	0.3	0.86(5)	60	1514513	pole 1: 143.104(5)	6.304	11.164(6)	-3.453(7)	0.158(6)	0.45(7)
							pole 2: 0.005(7)	0.587(9)	0.0	0.0	1.700(9)	4.90(6)
12(cb)	0.1	6.0	0.3	0.90(3)	60	973938	pole 1: 253.214(9)	6.384(5)	10.825(6)	-2.970(4)	0.156(6)	0.47(1)
							pole 2: 0.003	0.5	0.0	0.0	2.0	6.02(5)
12(cc)	0.1	7.0	0.3	0.97(6)	60	945883	pole 1: 324.065(9)	5.704(6)	12.104(1)	-0.435(6)	0.175(2)	0.57(0)
12(cd)	0.1	10.0	0.3	1.16(6)	60	926150	pole 1: 1687.226(1)	4.897(3)	14.378(1)	1.978(5)	0.204(1)	0.79(4)
13(aa)	0.15	0.71	0.5	0.63(4)	60	14028	pole 2: 1.951(4)	1.374(7)	0.0	0.0	0.727(4)	0.92(3)
							pole 3: 8.781(4)	10.792(1)	0.0	0.0	0.092(6)	0.11(7)
13(ab)	0.2	0.1	0.3	0.16(5)	60	12024	pole 2: 0.203(3)	0.553(8)	0.0	0.0	1.805(6)	0.99(3)
13(ac)	0.2	0.2	0.3	0.23(3)	60	12024	pole 2: 0.424(6)	0.797(9)	0.0	0.0	1.253(1)	0.97(4)
							pole 3: 6.137(6)	19.551(6)	0.0	0.0	0.051(1)	0.03(9)
13(ad)	0.2	0.3	0.3	0.28(5)	60	12024	pole 2: 0.648(1)	0.975(7)	0.0	0.0	1.024(8)	0.97(6)
							pole 3: 6.474(7)	15.734(2)	0.0	0.0	0.063(5)	0.06(0)
13(ba)	0.2	0.4	0.3	0.33(0)	60	11523	pole 2: 0.851(1)	1.112(4)	0.0	0.0	0.898(8)	0.98(8)
							pole 3: 0.725(5)	6.646(8)	0.0	0.0	0.150(4)	0.16(5)
13(bb)	0.2	0.5	0.3	0.36(9)	60	12024	pole 2: 1.097(9)	1.260(5)	0.0	0.0	0.793(2)	0.97(5)
							pole 3: 6.382(7)	11.197(1)	0.0	0.0	0.089(3)	0.10(9)
13(bc)	0.2	0.7	0.3	0.43(6)	60	12024	pole 2: 1.650(0)	1.530(3)	0.0	0.0	0.653(4)	0.95(0)
							pole 3: 12.455(4)	11.325(4)	0.0	0.0	0.088(2)	0.12(8)
13(bd)	0.2	1.0	0.3	0.52(1)	60	12024	pole 2: 2.035(7)	1.753(2)	0.0	0.0	0.570(3)	0.99(2)
							pole 3: 14.891(3)	8.355(3)	0.0	0.0	0.119(6)	0.20(8)
13(ca)	0.2	1.5	0.3	0.63(9)	60	9519	pole 2: 2.193(3)	2.000(9)	0.0	0.0	0.499(7)	1.06(4)
							pole 3: 51.449(1)	8.825(8)	0.0	0.0	0.113(3)	0.24(1)
13(cb)	0.2	2.0	0.3	0.73(8)	60	12024	pole 2: 1.450(7)	1.971(0)	0.0	0.0	0.507(3)	1.24(8)

Table continues on the next page

Table S3: Continuation from previous page

Figure	$c$ (mol/L)	$\lambda_B$ (nm)	$\sigma$ (nm)	$\sigma/\lambda_D$	$L$ (nm)	$N_g$	$a$ (1)	$b$ (1/nm)	$c$ (1/nm)	$d$ (1)	$\lambda$ (nm)	$\lambda/\lambda_D$
13(cc)	0.2	2.5	0.3	0.82(5)	60	12024	pole 3: 146.587(5) pole 2: 0.697(2) pole 3: 592.819(5)	9.884(5) 1.765(7) 12.562(7)	0.0 0.0 0.0	0.0 0.0 0.0	0.101(1) 0.566(3) 0.079(6)	0.24(8) 1.55(7) 0.21(8)
13(cd)	0.2	3.0	0.3	0.90(3)	60	12024	pole 1: 450.682(2) branch: 0.199(6)	10.787(9) 0.978(3)	8.051(5) 0.0	-3.111(1) 0.0	0.092(6) 1.022(1)	0.27(9) 3.07(9)
14(aa)	0.2	4.0	0.3	1.04(3)	60	12024	pole 1: 1192.387(2) pole 2: 0.068(0)	10.512(7) 1.227(2)	10.451(3) 0.0	2.429(2) 0.0	0.095(1) 0.814(8)	0.33(0) 2.83(4)
14(ab)	0.2	5.0	0.3	1.16(6)	60	12024	pole 1: 118.493(7)	6.515(5)	10.280(7)	-3.012(1)	0.153(4)	0.59(6)
14(ac)	0.2	6.0	0.3	1.27(8)	60	12024	pole 1: 111.605(4)	5.559(8)	11.310(5)	-0.137(7)	0.179(8)	0.76(6)
14(ad)	0.2	7.0	0.3	1.38(0)	60	12024	pole 1: 130.494(6)	4.814(8)	12.426(4)	-0.545(0)	0.207(6)	0.95(5)
14(ba)	0.2	10.0	0.3	1.65(0)	60	9823	pole 1: 470.323(5)	4.299(5)	14.446(2)	1.960(6)	0.232(5)	1.27(9)
14(bb)	0.3	0.71	0.3	0.53(8)	30	16533	pole 2: 1.604(7) pole 3: 3.285(9)	1.849(7) 7.395(8)	0.0 0.0	0.0 0.0	0.540(6) 0.135(2)	0.97(0) 0.24(2)
14(bc)	0.5	0.1	0.3	0.26(0)	60	3808	pole 2: 0.213(8) pole 3: 0.301(7)	0.890(0) 24.915(5)	0.0 0.0	0.0 0.0	1.123(5) 0.040(1)	0.97(7) 0.03(4)
14(bd)	0.5	0.2	0.3	0.36(9)	60	3307	pole 2: 0.457(5) pole 3: 4.057(7)	1.282(4) 25.408(5)	0.0 0.0	0.0 0.0	0.779(7) 0.039(3)	0.95(9) 0.04(8)
14(ca)	0.5	0.3	0.3	0.45(1)	60	3307	pole 2: 0.698(1) pole 3: 7.395(6)	1.561(3) 17.103(5)	0.0 0.0	0.0 0.0	0.640(4) 0.058(4)	0.96(4) 0.08(8)
14(cb)	0.5	0.4	0.3	0.52(1)	60	3808	pole 2: 0.967(8) pole 3: 2.102(7)	1.819(8) 11.397(8)	0.0 0.0	0.0 0.0	0.549(4) 0.087(7)	0.95(5) 0.15(2)
14(cc)	0.5	0.5	0.3	0.58(3)	60	3307	pole 2: 1.272(9) pole 3: 3.166(3)	2.061(8) 11.415(1)	0.0 0.0	0.0 0.0	0.485(0) 0.087(6)	0.94(3) 0.17(0)
14(cd)	0.5	0.7	0.3	0.69(0)	60	3307	pole 2: 1.892(3) pole 3: 6.725(5)	2.481(1) 10.919(3)	0.0 0.0	0.0 0.0	0.403(0) 0.091(5)	0.92(7) 0.21(0)
15(aa)	0.5	1.0	0.3	0.82(5)	60	3307	pole 2: 2.469(6) pole 3: 7.180(4)	2.915(7) 7.895(0)	0.0 0.0	0.0 0.0	0.342(9) 0.126(6)	0.94(3) 0.34(8)
15(ab)	0.5	1.5	0.3	1.01(0)	60	3150	pole 2: 1.643(2) pole 3: 26.571(0)	3.019(5) 8.087(0)	0.0 0.0	0.0 0.0	0.331(1) 0.123(6)	1.11(5) 0.41(6)
15(ac)	0.5	2.0	0.3	1.16(6)	60	3142	pole 1: 51.277(8) pole 2: 1.482(8)	8.657(4) 3.247(3)	4.037(8) 0.0	-1.387(5) 0.0	0.115(5) 0.307(9)	0.44(9) 1.19(7)
15(ad)	0.5	3.0	0.3	1.42(9)	60	3170	pole 1: 27.267(1)	5.131(2)	10.776(9)	-0.162(3)	0.194(8)	1.19(8)
15(ba)	0.5	5.0	0.3	1.84(5)	60	3307	pole 1: 48.144(1)	4.902(3)	11.867(8)	2.585(3)	0.203(9)	1.37(4)
15(bb)	0.5	6.0	0.3	2.02(1)	60	3307	pole 1: 54.675(0)	4.206(7)	12.909(0)	-0.932(5)	0.237(7)	1.72(9)
15(bc)	0.5	7.0	0.3	2.18(3)	60	3307	pole 1: 101.867(8)	3.511(4)	14.494(0)	-1.220(7)	0.284(7)	2.47(6)
15(bd)	0.5	10.0	0.3	2.60(9)	60	3117	pole 2: 2.241(4) pole 3: 2.672(9)	3.064(3) 9.736(3)	0.0 0.0	0.0 0.0	0.326(3) 0.102(7)	0.89(4) 0.28(1)
15(ca)	0.7	0.71	0.3	0.82(2)	30	15531	pole 1: 10.701(1) pole 2: 2.996(8)	4.625(9) 3.912(5)	4.164(2) 0.0	0.322(3) 0.0	0.216(1) 0.255(5)	0.94(6) 0.83(7)
15(cb)	0.98	$\approx 1.2918$	0.4	1.75(0)	30	160821	pole 3: 3.273(1) pole 1: 17.862(9)	26.018(4) 4.876(8)	0.0 11.124(8)	0.0 -0.348(2)	0.038(4) 0.205(0)	0.12(5) 1.78(3)
15(cc)	1.0	0.71	0.3	0.98(3)	30	16533	pole 2: 2.996(8) pole 3: 3.273(1)	3.912(5) 26.018(4)	0.0 0.0	0.0 0.0	0.255(5) 0.038(4)	0.83(7) 0.12(5)
15(cd)	1.0	5.0	0.3	2.60(9)	20	8016	pole 1: 17.862(9)	4.876(8)	11.124(8)	-0.348(2)	0.205(0)	1.78(3)
16(aa)	1.12	$\approx 0.8358$	0.294	1.10(6)	30	163829	pole 1: 16.714(8) pole 2: 8.671(2)	10.259(5) 5.428(9)	5.415(1) 0.0	0.833(5) 0.0	0.097(4) 0.184(1)	0.36(6) 0.69(3)
16(ab)	1.5	0.71	0.3	1.20(4)	30	14529	pole 2: 6.261(2)	5.601(0)	0.0	0.0	0.178(5)	0.71(6)
16(ac)	1.5	$\approx 1.6239$	0.4	2.42(8)	30	108266	pole 1: 5.838(1)	3.883(4)	5.664(8)	-0.254(0)	0.257(5)	1.56(3)
16(ad)	1.97	$\approx 2.1051$	0.4	3.16(8)	30	51051	pole 1: 4.062(1)	3.320(0)	6.466(0)	-0.398(4)	0.301(1)	2.38(5)
16(ba)	2.0	0.71	0.3	1.39(0)	30	13527	pole 2: 57.646(2)	9.088(6)	0.0	0.0	0.110(0)	0.50(9)
16(bb)	2.0	3.0	0.3	2.85(8)	20	8016	pole 1: 9.014(8)	5.675(8)	9.864(1)	2.618(6)	0.176(1)	1.67(8)
16(bc)	2.0	5.0	0.3	3.69(0)	20	8016	pole 1: 9.760(4)	4.491(6)	11.538(5)	2.525(0)	0.222(6)	2.73(8)
16(bd)	2.04	$\approx 0.9799$	0.294	1.61(6)	30	53185	pole 1: 9.705(2)	6.490(3)	5.209(8)	-2.788(4)	0.154(0)	0.84(7)
16(ca)	2.5	0.71	0.5	2.59(1)	30	9519	pole 1: 3.680(7)	3.934(2)	5.344(8)	2.825(9)	0.254(1)	1.31(7)
16(cb)	2.5	$\approx 2.8419$	0.4	4.14(7)	30	11438	pole 1: 3.020(6)	2.782(4)	7.190(7)	2.596(3)	0.359(3)	3.72(6)
16(cc)	2.65	$\approx 3.1576$	0.4	4.50(0)	30	7237	pole 1: 2.684(2)	2.599(0)	7.463(9)	2.459(9)	0.384(7)	4.32(9)
16(cd)	2.98	$\approx 1.093$	0.294	2.06(3)	30	18652	pole 1: 6.898(5)	5.952(1)	6.647(0)	-3.029(1)	0.168(0)	1.17(9)
17(aa)	3.0	0.71	0.5	2.83(8)	30	6513	pole 1: 3.697(3) pole 2: 17.258(8)	3.921(9) 8.140(8)	5.705(1) 11.543(6)	-0.415(3) -2.362(4)	0.254(9) 0.122(8)	1.44(7) 0.69(7)
17(ab)	3.0	3.0	0.3	3.50(0)	20	5511	pole 1: 5.765(3)	5.088(8)	10.170(8)	2.608(1)	0.196(5)	2.29(3)
17(ac)	3.0	$\approx 3.7891$	0.4	5.24(5)	30	6432	pole 1: 2.770(9)	2.416(0)	7.760(8)	2.508(8)	0.413(8)	5.42(7)
17(ad)	3.0	5.0	0.3	4.51(9)	20	5511	pole 1: 6.431(9)	4.170(0)	11.682(1)	2.501(6)	0.239(8)	3.61(2)
17(ba)	3.13	$\approx 4.0598$	0.4	5.54(6)	30	13244	pole 1: 2.598(4)	2.312(5)	7.937(2)	-0.732(8)	0.432(4)	5.99(5)
17(bb)	3.5	0.71	0.3	1.83(9)	30	5511	pole 1: 7.251(4)	7.142(1)	5.724(8)	0.426(8)	0.140(0)	0.85(8)
17(bc)	4.0	0.71	0.3	1.96(6)	30	4509	pole 1: 6.103(9)	6.951(7)	6.150(9)	-2.745(5)	0.143(8)	0.94(2)
17(bd)	4.06	$\approx 1.2356$	0.294	2.56(1)	30	9330	pole 1: 4.861(3)	5.361(8)	7.994(8)	2.812(3)	0.186(5)	1.62(4)
17(ca)	4.5	0.71	0.3	2.08(5)	30	2004	pole 1: 6.588(7)	7.101(9)	6.623(0)	-2.853(8)	0.140(8)	0.97(8)
17(cb)	4.93	$\approx 1.3218$	0.294	2.91(9)	30	4824	pole 1: 2.690(8)	4.611(2)	8.503(7)	-0.358(6)	0.216(8)	2.15(3)
17(cc)	5.0	0.1	0.3	0.82(5)	20	5010	pole 2: 0.340(4) pole 3: 5.507(9)	3.138(2) 20.387(0)	0.0 0.0	0.0 0.0	0.318(6) 0.049(0)	0.87(6) 0.13(4)
17(cd)	5.0	0.2	0.3	1.16(6)	20	5010	pole 1: 5.816(9) pole 2: 1.299(6)	15.164(8) 5.084(8)	10.075(5) 0.0	-1.008(3) 0.0	0.065(9) 0.196(6)	0.25(6) 0.76(4)
18(aa)	5.0	0.3	0.3	1.42(9)	20	5010	pole 1: 4.343(4)	9.471(2)	6.624(0)	1.361(0)	0.105(5)	0.50(2)

Table continues on the next page

Table S3: Continuation from previous page

Figure	$c$ (mol/L)	$\lambda_B$ (nm)	$\sigma$ (nm)	$\sigma/\lambda_D$	$L$ (nm)	$N_g$	$a$ (1)	$b$ (1/nm)	$c$ (1/nm)	$d$ (1)	$\lambda$ (nm)	$\lambda/\lambda_D$
18(ab)	5.0	0.4	0.3	1.65(0)	20	5010	pole 2: 6.500(6)	8.006(4)	0.0	0.0	0.124(8)	0.59(5)
18(ac)	5.0	0.5	0.3	1.84(5)	20	5010	pole 1: 5.034(9)	7.163(5)	3.079(3)	2.041(6)	0.139(5)	0.76(7)
							pole 1: 3.996(0)	7.090(5)	6.518(5)	3.065(6)	0.141(0)	0.86(7)
							pole 2: 23.485(4)	14.274(7)	0.0	0.0	0.070(0)	0.43(0)
18(ad)	5.0	0.7	0.3	2.18(3)	20	4509	pole 1: 4.342(8)	6.569(6)	7.163(3)	0.083(7)	0.152(2)	1.10(7)
18(ba)	5.0	1.0	0.3	2.60(9)	20	4509	pole 1: 3.763(2)	5.887(6)	8.222(1)	-0.173(9)	0.169(8)	1.47(7)
18(bb)	5.0	1.5	0.3	3.19(5)	20	4008	pole 1: 3.055(0)	5.094(4)	9.263(6)	-0.408(2)	0.196(2)	2.09(0)
18(bc)	5.0	2.0	0.3	3.69(0)	20	4008	pole 1: 2.728(7)	4.587(9)	9.848(9)	2.665(7)	0.217(9)	2.68(1)
18(bd)	5.0	2.5	0.3	4.12(5)	20	4008	pole 1: 3.259(1)	4.537(1)	10.229(3)	2.663(7)	0.220(4)	3.03(1)
18(ca)	5.0	3.0	0.3	4.51(9)	20	4008	pole 1: 3.312(0)	4.331(0)	10.697(6)	2.579(1)	0.230(8)	3.47(8)
18(cb)	5.0	4.0	0.3	5.21(8)	20	4008	pole 1: 2.906(3)	3.813(5)	11.010(5)	-0.282(5)	0.262(2)	4.56(1)
18(cc)	5.0	5.0	0.3	5.83(4)	20	4008	pole 1: 3.213(2)	3.591(1)	11.874(1)	2.510(2)	0.278(4)	5.41(5)
18(cd)	5.0	6.0	0.3	6.39(1)	20	4008	pole 1: 3.372(7)	3.264(4)	12.340(6)	-0.630(6)	0.306(3)	6.52(6)
19(aa)	5.0	7.0	0.3	6.90(3)	20	4008	pole 1: 3.914(1)	3.032(5)	12.985(8)	2.291(0)	0.329(7)	7.58(8)
19(ab)	5.0	10.0	0.3	8.25(1)	20	4008	pole 1: 5.019(7)	2.315(1)	14.376(0)	1.966(6)	0.431(9)	11.88(0)
19(ac)	5.5	0.71	0.3	2.30(5)	30	2505	pole 1: 3.879(8)	6.401(5)	7.600(8)	-0.039(8)	0.156(2)	1.20(0)
19(ad)	6.0	0.71	0.3	2.40(8)	30	2505	pole 1: 3.658(9)	6.348(0)	7.893(3)	-0.105(9)	0.157(5)	1.26(4)
19(ba)	10.0	0.1	0.3	1.16(6)	20	1503	pole 2: 0.526(6)	4.884(2)	0.0	0.0	0.204(7)	0.79(6)
							pole 3: 11.281(9)	18.996(3)	0.0	0.0	0.052(6)	0.20(4)
19(bb)	10.0	0.7	0.3	3.08(7)	20	1503	pole 1: 1.894(5)	5.533(0)	9.585(7)	2.662(6)	0.180(7)	1.85(9)
19(bc)	10.0	1.0	0.3	3.69(0)	20	501	pole 1: 1.675(0)	4.850(5)	10.244(6)	-0.546(1)	0.206(1)	2.53(5)
19(bd)	10.0	1.5	0.3	4.51(9)	20	1503	pole 1: 1.911(6)	4.366(8)	10.887(3)	2.525(0)	0.228(9)	3.44(9)
19(ca)	10.0	2.0	0.3	5.21(8)	20	1002	pole 1: 1.847(5)	3.922(3)	11.293(7)	-0.640(3)	0.254(9)	4.43(4)
19(cb)	10.0	2.5	0.3	5.83(4)	20	1002	pole 1: 1.792(3)	3.605(8)	11.621(9)	2.464(5)	0.277(3)	5.39(3)
19(cc)	10.0	3.0	0.3	6.39(1)	20	1002	pole 1: 1.714(0)	3.345(0)	11.931(7)	2.370(3)	0.298(9)	6.36(8)
19(cd)	10.0	4.0	0.3	7.38(0)	20	1002	pole 1: 1.974(1)	3.123(6)	12.417(4)	2.264(0)	0.320(1)	7.87(5)
20(aa)	10.0	5.0	0.3	8.25(1)	20	501	pole 1: 1.861(9)	2.848(0)	12.764(2)	2.217(5)	0.351(1)	9.65(7)
20(ab)	10.0	6.0	0.3	9.03(8)	20	1002	pole 1: 1.822(6)	2.659(5)	13.024(4)	2.210(8)	0.376(0)	11.32(8)
20(ac)	10.0	7.0	0.3	9.76(3)	20	1002	pole 1: 1.939(5)	2.542(5)	13.316(2)	2.185(3)	0.393(3)	12.79(9)
20(ad)	10.0	10.0	0.3	11.66(9)	20	1002	pole 1: 1.974(9)	2.050(1)	14.182(6)	2.059(9)	0.487(7)	18.97(2)

- [S1] A. M. Smith, A. A. Lee, and S. P. Perkin, *The Journal of Physical Chemistry Letters* **7**, 2157 (2016).
- [S2] P. Debye and E. Hückel, *Physikalische Zeitschrift* **24**, 185 (1923).
- [S3] J.-P. Hansen and I. R. McDonald, *Theory of Simple Liquids*, 4th ed. (Elsevier, Oxford, 2013).
- [S4] P. Cats, R. Evans, A. Härtel, and R. van Roij, *The Journal of Chemical Physics* **154**, 124504 (2021).
- [S5] F. Weik, R. Weeber, K. Szuttor, K. Breitsprecher, J. de Graaf, M. Kuron, J. Landsgesell, H. Menke, D. Sean, and C. Holm, *The European Physical Journal Special Topics* **227**, 1789 (2019).
- [S6] H. C. Andersen, J. D. Weeks, and D. Chandler, *Physical Review A* **4**, 1597 (1971).
- [S7] J. D. Weeks, D. Chandler, and H. C. Andersen, *The Journal of Chemical Physics* **54**, 5237 (1971).
- [S8] R. W. Hockney and J. W. Eastwood, *Computer simulation using particles* (IOP, London, 1988).
- [S9] P. Attard, C. P. Ursenbach, and G. N. Patey, *Physical Review A* **45**, 7621 (1992).
- [S10] R. Kjellander and D. J. Mitchell, *Chemical Physics Letters* **200**, 76 (1992).
- [S11] R. Evans, J. R. Henderson, D. C. Hoyle, A. O. Parry, and Z. A. Sabeur, *Molecular Physics* **80**, 755 (1993).
- [S12] R. Evans, R. J. F. Leote de Carvalho, J. R. Henderson, and D. C. Hoyle, *The Journal of Chemical Physics* **100**, 591 (1994).
- [S13] R. J. F. Leote de Carvalho and R. Evans, *Molecular Physics* **83**, 619 (1994).
- [S14] F. Coupette, A. A. Lee, and A. Härtel, *Physical Review Letters* **121**, 075501 (2018).
- [S15] J. Ennis, R. Kjellander, and D. J. Mitchell, *The Journal of Chemical Physics* **102**, 975 (1995).
- [S16] J. Ulander and R. Kjellander, *The Journal of Chemical Physics* **114**, 4893 (2001).
- [S17] P. González-Mozuelos, G. I. Guerrero-García, and M. Olvera de la Cruz, *The Journal of Chemical Physics* **139**, 064709 (2013).
- [S18] R. Evans, *Advances in Physics* **28**, 143 (1979).
- [S19] A. Härtel, *Journal of Physics: Condensed Matter* **29**, 423002 (2017).
- [S20] R. Roth and D. Gillespie, *Journal of Physics: Condensed Matter* **28**, 244006 (2016).
- [S21] M. Bültmann and A. Härtel, *Journal of Physics: Condensed Matter* **34**, 235101 (2022).
- [S22] Y. Rosenfeld, *Physical Review Letters* **63**, 980 (1989).
- [S23] R. Roth, *Journal of Physics: Condensed Matter* **22**, 063102 (2010).
- [S24] H. Hansen-Guus and R. Roth, *Journal of Physics: Condensed Matter* **18**, 8413 (2006).
- [S25] J. K. Percus, *Physical Review Letters* **8**, 462 (1962).
- [S26] H. L. Frisch and J. L. Lebowitz, *The Equilibrium Theory of Classical Fluids: a Lecture Note and Reprint volume* (WA Benjamin, New York, 1964).
- [S27] J. G. Kirkwood, *The Journal of Chemical Physics* **7**, 919 (1939).